



HAL
open science

Troposphere-to-mesosphere microphysics of carbon dioxide ice clouds in a Mars Global Climate Model

Anni Määttänen, Christophe Mathé, Joachim Audouard, Constantino Listowski, E. Millour, Francois, Forget, F. González-Galindo, Lola Falletti, D. Bardet, L. Teinturier, et al.

► **To cite this version:**

Anni Määttänen, Christophe Mathé, Joachim Audouard, Constantino Listowski, E. Millour, et al.. Troposphere-to-mesosphere microphysics of carbon dioxide ice clouds in a Mars Global Climate Model. *Icarus*, 2022, 385 (October), pp.115098. 10.1016/j.icarus.2022.115098 . hal-03681679

HAL Id: hal-03681679

<https://hal.science/hal-03681679v1>

Submitted on 30 May 2022

HAL is a multi-disciplinary open access archive for the deposit and dissemination of scientific research documents, whether they are published or not. The documents may come from teaching and research institutions in France or abroad, or from public or private research centers.

L'archive ouverte pluridisciplinaire **HAL**, est destinée au dépôt et à la diffusion de documents scientifiques de niveau recherche, publiés ou non, émanant des établissements d'enseignement et de recherche français ou étrangers, des laboratoires publics ou privés.

Troposphere-to-mesosphere microphysics of carbon dioxide ice clouds in a Mars Global Climate Model

A. Määttänen^{a,*}, C. Mathé^{a,c}, J. Audouard^{a,1}, C. Listowski^{b,2}, E. Millour^c, F. Forget^c, F. González-Galindo^d, L. Falletti^a, D. Bardet^e, L. Teinturier^f, M. Vals^b, A. Spiga^{c,8} and F. Montmessin^b

^aLATMOS/IPSL, Sorbonne université, UVSQ Université Paris-Saclay, CNRS, Paris, France

^bLATMOS/IPSL, UVSQ Université Paris-Saclay, Sorbonne université, CNRS, Guyancourt, France

^cLaboratoire de Météorologie Dynamique / Institut Pierre-Simon Laplace (LMD/IPSL), Sorbonne Université, Centre National de la Recherche Scientifique (CNRS), École Polytechnique, École Normale Supérieure (ENS), Paris, France

^dInstituto de Astrofísica de Andalucía-CSIC, Granada, Spain

^eSchool of Physics and Astronomy, University of Leicester, Leicester, UK

^fLESIA, Observatoire de Paris, Université PSL, CNRS, Sorbonne Université, Univ. Paris Diderot, Sorbonne Paris Cité, Meudon, France

⁸Institut Universitaire de France (IUF), Paris, France

ARTICLE INFO

Keywords:

Mars
clouds
microphysics
modeling

ABSTRACT

We have implemented full CO₂ ice cloud microphysics into the LMD Mars Global Climate Model (MGCM) and we have conducted the first global simulations. The microphysical model implementation follows the modal scheme used for water ice cloud microphysics in the MGCM, but includes specific aspects that need to be accounted for when dealing with CO₂ ice clouds. These include nucleation of CO₂ on water ice crystals and CO₂ condensation theory adapted for the Martian conditions. The model results are compared to available observations globally, and separately for polar regions and equatorial mesosphere. The observed seasonal and latitudinal variability of the CO₂ ice clouds is in general reproduced. The polar regions are covered by CO₂ ice clouds during the winter as observed. Instead of forming only in the lowest 10-15 km of the atmosphere, they extend up to several tens of kilometers above the surface in the model, dictated by the modeled temperature structure. We have also quantified the contribution of the cloud microphysics to the surface CO₂ ice deposits. Snowfall from these clouds contributes up to 10% of the atmosphere-surface ice flux in the polar regions in our simulations, in the range that has been indirectly deduced from observations. In the mesosphere, notable amounts of CO₂ ice clouds form only when water ice crystals are used as condensation nuclei in addition to dust particles, and their spatial distribution is in agreement with observations. The mesospheric temperature structure, dominated by tides, dictates the longitudinal and seasonal distribution of these clouds. The seasonal and local time variations of the clouds are not fully reproduced by the model. There is a long pause in CO₂ ice cloud formation in the model around the aphelion season, but clouds have been observed during this period, although with a lower apparition frequency. Modeled mesospheric clouds form mainly during the night and in the morning, whereas during the daytime, when most of the cloud observations have been made, the model rarely predicts clouds. These discrepancies could be explained by the strong dependence of the cloud formation process on mesospheric temperatures that are themselves challenging to reproduce and sensitive to the MGCM processes and parameters. The rare possibilities for nighttime observations might also bias the observational climatologies towards daytime detections. Future developments of the model consist in the inclusion of a possible exogenous condensation nucleus source in the mesosphere and the radiative effect of CO₂ ice clouds.

1. Introduction

Carbon dioxide is the main atmospheric gas on Mars, and condenses as ice on the polar caps and as clouds in the atmosphere. These clouds are an important element of the Martian CO₂ cycle, but so far their role has not been well quantified. Observations of CO₂ ice clouds were rare until about twenty years ago, and detailed modeling of CO₂ ice

*Corresponding author

 anni.maattanen@latmos.ipsl.fr (A. Määttänen)

ORCID(s):

¹Currently at: WPO, Paris, France

²Currently at: CEA/DAM/DIF, F-91297 Arpajon, France

cloud microphysics was slowed down due to the lack of observations of cloud properties. The increasing amount of observational datasets during the last decade has enabled the development of detailed CO₂ microphysics for Mars.

Around the turn of the century, the Mars Orbiter Laser Altimeter (MOLA) on the Mars Global Surveyor (MGS) mission observed, while measuring the Martian topography in unprecedented detail, strong laser echoes within the polar night not coming from the surface. These echoes were attributed to the laser light being reflected from the tops of CO₂ ice clouds (Pettengill and Ford, 2000; Ivanov and Muhleman, 2001) that had been predicted to form within the winter polar night at both poles (Forget et al., 1995; Forget et al., 1998). MOLA mapped these cloud top echoes, revealing that the clouds were very thick, with top altitudes mainly below 10 km, but reaching even 20 km (Ivanov and Muhleman, 2001). MOLA data also revealed sloping fronts reminiscent of wave structures, and allowed even for estimating the horizontal and vertical wavelengths corresponding to buoyancy waves (Pettengill and Ford, 2000). Based on MOLA observations, Ivanov and Muhleman (2001) concluded that CO₂ ice snowfall would not significantly contribute to the CO₂ ice cap. All of the aspects of the MOLA cloud climatology were discussed by Neumann et al. (2003).

A decade later the Mars Climate Sounder (MCS) radiometer on the Mars Reconnaissance Orbiter (MRO) mission probed the Martian polar nights and was able to shed more light on the questions related to the CO₂ condensation in the polar night. MCS measured the radiative cooling rates in the polar night and, with hypotheses on particle sizes, deduced that 3–20% by mass of the seasonal polar cap CO₂ might be deposited by snowfall coming from the lowest atmosphere (below 4 km) (Hayne et al., 2012, 2014). The estimated sedimentation velocities indicated that the crystals likely fell to the ground between the frequent observations by the MCS, meaning that the cloud must have been constantly replenished. To explain this, a potential positive feedback between radiative cooling and CO₂ ice cloud crystal formation was pointed out (Hayne et al., 2014); this feedback, where formation of CO₂ clouds increases radiative cooling that in turn decreases temperatures and induces further cloud formation, would reinforce the formation of the clouds until either the supersaturation or the ice nuclei have been depleted.

The observations by MOLA and MCS give the only observational constraints we have on the polar CO₂ ice clouds: occurrences, cloud top heights and slope angles, estimates on particle sizes and optical thicknesses, radiative cooling rates that can be converted into condensed mass, and estimates on the fraction of the seasonal CO₂ cap deposited as snowfall (instead of direct condensation onto the ground). All of the estimates require certain assumptions (particle sizes for example) that are difficult to constrain without microphysical modeling.

Mesospheric clouds were revealed by two instruments on the MGS mission, the Mars Orbiting Camera (MOC) and the Thermal Emission Spectrometer (TES), that detected aerosol layers in the mesosphere in equatorial limb observations around the summer solstice (Clancy et al., 2007). The SPICAM instrument on Mars Express mission (MEX) detected four very high-altitude aerosol layers (around 100 km) in stellar occultation in low southern latitudes, adjacent to cold pockets supersaturated with respect to CO₂ ice (Montmessin et al., 2006). Then OMEGA instrument on MEX detected, spectroscopically for the first time, a clear signature of CO₂ ice crystals at 4.26 μm in its near-IR nadir images in the tropics (Montmessin et al., 2007). The signature was shown to come from micrometer-sized CO₂ crystals lofted above 40 km altitude in the Martian atmosphere (Montmessin et al., 2007). The first climatology of the mesospheric clouds on Mars was constructed based on these observations (MOC, TES, SPICAM, OMEGA), but only some of which (OMEGA) allowed for the identification of the cloud composition. Some of these observations could be used for estimating the altitudes, optical thicknesses and effective particle sizes (see the review by Määttä et al., 2013).

The first multi-annual climatologies were completed by the analysis of three Mars years of MEX data with OMEGA (Määttä et al., 2010) and High Resolution Stereo Camera (HRSC, Scholten et al., 2010). These studies revealed more details on the climatology of these clouds. They form mainly in the tropics during the northern spring and summer in preferred longitude ranges. Also midlatitude clouds forming in the local autumn were observed on both hemispheres. HRSC with its stereo capabilities revealed the altitudes and the east-west displacement speeds of these clouds; this provided very rare and valuable data on mesospheric wind speeds.

Other climatologies have been published after these first discoveries: the Compact Reconnaissance Imaging Spectrometer for Mars (CRISM) instrument on MRO distinguished CO₂ ice clouds from water ice clouds by the absence of water ice absorption signatures (Vincendon et al., 2011) and the MCS instrument mapped high-altitude detached layers without definitive composition identification (Sefton-Nash et al., 2013). The latest additions to the climatologies come from the Imaging Ultraviolet Spectrograph (IUVS) instrument on the MAVEN mission that observed mesospheric detached layers at limb (Stevens et al., 2017) and two putative CO₂ ice clouds in stellar occultation (Jiang et al., 2019), from the Planetary Fourier Spectrometer (PFS) on MEX that measures the same

117 4.26 μm CO₂ ice scattering peak as OMEGA (Aoki et al., 2018), and from CRISM/MRO limb profiles providing
 118 composition of mesospheric aerosols as well (Clancy et al., 2019).

119 Several modeling studies dealing with CO₂ ice clouds have been published, ranging from Global Climate Model
 120 (GCM) simulations with simplified condensation parametrizations (Forget et al., 1998; Kuroda et al., 2013) through
 121 one-dimensional modeling of convective clouds including radiative effects (Colaprete et al., 2003) and two-dimensional
 122 modeling of lee wave clouds (Tobie et al., 2003) up to global simulations with more refined microphysics (Colaprete
 123 et al., 2008). These earlier CO₂ ice cloud modeling studies (Tobie et al., 2003; Colaprete et al., 2008; Kuroda et al.,
 124 2013) tested ideas on cloud formation but suffered from limitations due to simplified physics and/or model boundaries
 125 such as a low model top. The column model of Listowski et al. (2014) used refined microphysics adapted for the Martian
 126 conditions (Listowski et al., 2013). Despite the limitations of a one-dimensional model, (Listowski et al., 2014) showed
 127 that an additional source of condensation nuclei (CN) was required in the mesosphere. One study of cloud-resolving
 128 simulations on CO₂ condensation has been performed for the Early Mars climate (Yamashita et al., 2016), but none
 129 in the current conditions of Martian polar regions. Moreover, the respective roles of topography (Tobie et al., 2003;
 130 Colaprete and Toon, 2002) and convection (Colaprete et al., 2008) in driving cloud formation and snowfall in the polar
 131 regions remain to be determined, as does the coupling of CO₂ and H₂O cycles through heterogeneous nucleation of
 132 CO₂ on H₂O crystals. Recent studies have also shown that the CO₂ condensation at the poles determines the structure
 133 of the polar vortex (Toigo et al., 2017).

134 The necessary ingredients giving rise to the formation of mesospheric clouds have been studied with GCMs with
 135 and without microphysics (Colaprete et al., 2008; González-Galindo et al., 2011) and with idealized, theoretical studies
 136 (Spiga et al., 2012). Some studies (Colaprete et al., 2008; Yiğit et al., 2015) failed in reproducing the observed
 137 distribution of mesospheric clouds, but the studies done with the earlier versions of the modeling tools of our
 138 group (González-Galindo et al., 2011; Spiga et al., 2012) pioneered in confirming that the mesospheric clouds very
 139 probably form in supersaturated pockets created by the superposition of planetary scale thermal tides and gravity
 140 waves propagating to the mesosphere. However, in the cited studies (González-Galindo et al., 2011; Spiga et al., 2012)
 141 planetary and mesoscale processes were not coupled, and no supersaturation was attained during daytime in the global
 142 model because the gravity wave effect on the temperatures was not accounted for.

143 Recently our group has developed a state-of-the-art microphysical column (1D) model for CO₂ ice clouds
 144 (Listowski et al., 2013, 2014). The coupling of this model to the LMD Mars Global Climate Model (the acronym
 145 MGCM is used hereafter), jointly developed by several laboratories, including LATMOS, LMD, and IAA (Forget
 146 et al., 1999; Navarro et al., 2014), has now been achieved by our team. Today, this MGCM is the most advanced tool
 147 available for studying the CO₂ ice clouds on Mars thanks to its refined microphysics, high model top (~ 120 km, more
 148 details in 2.3) and the proper handling of CO₂ condensation in the polar regions. Other important processes related to
 149 CO₂ ice clouds, such as their radiative effect, will be investigated in future studies. In this paper we describe the new
 150 CO₂ ice cloud microphysical model coupled with the MGCM and the first reference simulations. These simulations
 151 have been performed in order to investigate different open questions related to CO₂ ice clouds on Mars, such as: the
 152 role of the CO₂ ice clouds in the formation of the polar ice caps through snowfall, the influence of water ice crystals as
 153 CN for CO₂ ice clouds, and the importance of the thermal structure and CN sources on the formation of mesospheric
 154 CO₂ ice clouds. The model results are interpreted in order to shed light on these questions.

155 2. Methods

156 2.1. Microphysical model description

157 The microphysical CO₂ ice cloud model is based on the one developed by Listowski et al. (2013, 2014) and
 158 extensively tested in one dimension in the case of mesospheric CO₂ ice clouds (Listowski et al., 2014). The model
 159 includes the primary microphysical processes ruling the formation and evolution of CO₂ ice clouds on Mars: nucleation
 160 on dust particles (and here also on water ice crystals), and condensation/evaporation accounting for the particular
 161 conditions in which phase transitions of CO₂ happen on Mars (highly supersaturated, near-pure vapor in the kinetic
 162 regime: see details in Listowski et al. (2013)). As a one-dimensional (1D) model, it also accounted for sedimentation.
 163 The model of Listowski et al. (2013, 2014) is a sectional model, which means that the model discretizes the particle
 164 size distribution in size bins and calculates the effect of the microphysical processes on the number concentration in
 165 each size bin: in this way, the form of the size distribution can freely evolve. This method can be computationally
 166 expensive, but its cost in a 1D framework is not prohibitive.

167 The implementation of the CO₂ microphysics to the MGCM follows the modal scheme (or the moment method) that
 168 we will describe briefly in the following, used already for the MGCM implementation of water ice cloud microphysics
 169 (Madeleine et al., 2014; Navarro et al., 2014).

170 2.1.1. The moment method

The moment method, used in so-called modal aerosol models, describes the particle size distribution with the help
 of its integral properties. The form of the size distribution is fixed with a well-known function that adequately follows
 the actual shape of the distribution. The log-normal law is commonly used in aerosol modeling (Jacobson, 2005) since
 it describes the shape of natural particle size distributions in a fairly realistic way, and it also has advantages in being
 easy to integrate. The moments of a size distribution are defined as:

$$M_k = \int_0^{\infty} r^k n(r) dr. \quad (1)$$

where M_k is the k th order moment, r is the radius and $n(r)$ is the number concentration of the particles of size r . For
 $k = 0$ the integral gives the total number of particles, $k = 1$ the average radius of the distribution, and the second and
 third order moments ($k = 2$, $k = 3$) are proportional to the total surface area and the total volume of the distribution.
 When certain properties of the size distribution are fixed (such as the standard deviation, and of course the shape), the
 full size distribution can be reconstructed from the moments whose values are known (for example, the average radius,
 the total number and volume (or mass) of the particles). By using the log-normal distribution, we can rewrite:

$$M_k = N_{\text{tot}} r_g^k \exp\left(\frac{k^2 \ln^2(\sigma_g)}{2}\right) = M_0 r_g^k \exp\left(\frac{k^2 \ln^2(\sigma_g)}{2}\right) \quad (2)$$

171 where M_0 is equal to the total number of particles of the distribution, r_g is the geometric average radius and
 172 σ_g the corresponding standard deviation. Equation (2) shows how the moments of the log-normal distribution are
 173 interdependent. This equation (2) allows us to calculate the other properties of the distribution from the ones we know.
 174 Using the moment method the number of tracers to be transported in the model can be reduced to a strict minimum that
 175 still adequately allows for a posterior description of the full size distribution. The shortcomings of this method are the
 176 fixed shape of the size distribution, which means that for a multi-modal size distribution of the same composition (the
 177 case of Venus: Knollenberg and Hunten, 1980) one would need to define and follow separately the properties of each
 178 mode in the model. For Mars, the size distributions for each particle type (dust, water ice crystals, CO₂ crystals) are
 179 here considered unimodal. Bimodal particle distributions have been suggested as well. Fedorova et al. (2014) provide
 180 evidence of such a distribution on Mars, however, without a possibility to unambiguously identify the composition
 181 of each mode. Thus, there is a possibility of a bimodal dust distribution in the Martian atmosphere, but the current
 182 MGCM version we are using is based on the unimodal hypothesis.

183 When using the moment method, the microphysical processes describe the evolution of the specific moments that
 184 have been selected as tracers (transported variables). In our case, the model dynamics transport moments that describe
 185 the number and the mass (mass mixing ratio) of the particles: thus the process equations need to describe the tendencies
 186 of these variables. These processes are described in the following sections.

187 2.1.2. Nucleation

188 Due to the abundant CN in the Martian atmosphere and the extremely low temperatures (high supersaturations)
 189 required for homogeneous nucleation (Määttänen et al., 2010), we are only accounting for heterogeneous nucleation in
 190 the model. Contrary to the rest of the microphysics code, the nucleation subroutine discretizes the CN size distribution
 191 into 100 size classes and calculates the nucleation rate separately for each size class (using Classical Nucleation Theory:
 192 for Martian nucleation see Määttänen et al., 2005; Määttänen et al., 2007; Määttänen and Douspis, 2014). Then the
 193 nucleation probability, giving the fraction of activated particles when integrated over the size classes, is calculated, and
 194 the fraction of activated particles is transferred to the CN tracer. The choice of the number of size classes was chosen
 195 after a series of tests that showed that about 100 size bins were needed to approach the exact solution (calculated using
 196 thousands of size bins) of the number of activated CN.

197 The potential CN for CO₂ ice on Mars are the omnipresent mineral dust particles, the water ice crystals that may
 198 have previously formed at higher temperatures and the plausible mesospheric CN formed as a consequence of meteor
 199 ablation in the middle atmosphere. The nature of the latter has been discussed, for example, in Listowski et al. (2014),

200 Crismani et al. (2017) and Plane et al. (2018). The dust tracer is the main CN source, containing the mineral dust
 201 particles. If the dust is activated as CN, the activated number and mass are transferred from the dust tracer to a dust CN
 202 tracer. Since CO₂ can also nucleate on water ice crystals, they can also be considered as potential CN when calculating
 203 CO₂ nucleation. This process has been included in the model through an option that can be activated or deactivated.
 204 When this option is activated, we expect more CO₂ ice clouds to form since with this option a greater number of CN
 205 will be available. This will probably have an effect at the winter poles where thick water ice clouds form, and in the
 206 mesosphere that the mineral dust lofted from the surface hardly reaches. The model thus now includes new tracers that
 207 follow the water ice crystals activated as CN and the dust CN captured within those water ice crystals. These quantities
 208 are kept in memory so that when CO₂ ice crystals sublime, the water ice crystals and the dust CN within them are
 209 returned to the corresponding tracers and all quantities are conserved.

210 An important parameter for nucleation is the so-called contact parameter m that describes the affinity of the surface
 211 material and the nucleating substance. It is defined as the cosine of the contact angle, which, theoretically, is the angle
 212 between two interfaces: the interface between the vapor and the condensed phase and the one between the condensed
 213 phase and the condensation nucleus. The smaller the contact angle, the more wettable the CN surface, the larger the
 214 contact parameter, and nucleation is favored. This parameter needs to be derived from nucleation experiments and it
 215 has been measured for the Martian substances. Until recently, the only measurements made for CO₂ ice nucleation were
 216 from Glandorf et al. (2002). In their experiments CO₂ nucleated on a layer of water ice, and revealed a contact parameter
 217 highly favorable for CO₂ nucleation: their average contact angle was $m = 0.952$. The crystalline structures of ices are
 218 very similar and in theory this close structural match facilitates nucleation. However, since this contact parameter
 219 value was the only one available for CO₂ nucleation, it was used also for describing CO₂ nucleation on mineral dust.
 220 Fairly recently, Nachbar et al. (2016) performed CO₂ nucleation experiments on CN that are analogous to Martian dust
 221 and to the particles formed after meteor ablation (so-called Meteoric Smoke Particles, MSPs). They found that the
 222 actual contact parameters on these realistic CN were much lower ($m = 0.78$) than the one from Glandorf et al. (2002),
 223 meaning that CO₂ nucleation on mineral dust and MPS analogs might be much more difficult than predicted with the
 224 older m values. In our simulations only the Glandorf et al. (2002) value $m = 0.952$ is used for both dust and water
 225 ice. This is because: a) due to temperature conditions and water vapor concentrations on Mars, water ice formation
 226 on dust very probably happens nearly always before CO₂ ice nucleates, and b) iron oxides are hydrophilic and adsorb
 227 water molecules on their surfaces in low temperature conditions, later forming ice (see Duft et al., 2019, and references
 228 therein), and thus CO₂ ice probably always nucleates on CN closely resembling water ice.

229 It should be kept in mind that the simulation including water ice as CN should be considered as the most realistic
 230 reference run.

231 2.1.3. Condensation/sublimation

232 Condensation and sublimation are described by three coupled equations ruling transfers of mass and heat through
 233 the profiles of temperature and vapor concentration as a function of distance from the surface of the crystal (Listowski
 234 et al., 2013). In the case of a condensing trace gas (like water vapor on the Earth or on Mars), one of the equations,
 235 linking the ambient saturation ratio to the one at the surface of the crystal can be linearized, providing an analytical
 236 solution to the system of equations. This is possible when it can be assumed that the crystal is in thermodynamical
 237 equilibrium with its surroundings, so the temperature of the crystal surface is not very different from the ambient gas
 238 temperature. This is the well known approach used in practically all cloud models for any planet. However, in the case
 239 of condensation of a highly supersaturated near-pure gas, like CO₂ in the mesosphere of Mars, the assumption of a
 240 thermalized crystal does not hold anymore, but a large temperature difference can develop, and the equation can not be
 241 linearized. In such a case an iterative solution needs to be implemented, as was done in Listowski et al. (2013, 2014).
 242 Here (see Appendix B), we have performed a scale analysis of the equation that needs to be solved iteratively (eq. (6) of
 243 Listowski et al., 2014) and show that it can be reduced to a form that can be solved analytically. The difference between
 244 the exact and the approximative solution is $\leq 0.6\%$ for a large range of conditions. This new, analytical method for
 245 solving the growth rates is applied in the MGCM now to avoid using an iterative (and potentially time-consuming)
 246 solution.

247 2.1.4. Sedimentation

248 All particles are sedimented in the model. We calculate sedimentation of CO₂ ice crystals just like it is done
 249 for water ice crystals in the model, as described in Navarro et al. (2014) and Montmessin et al. (2004). The Stokes-
 250 Cunningham relationship is used for calculating the fall speed. An effective fall radius $r_{\text{sed}} = r_c(1 + v_{\text{eff}})^3$ is used in

251 this calculation since it describes the sedimentation process in a more realistic manner than the mass mean radius r_c .
 252 Sedimentation of CO₂ crystals is calculated for each microphysical subimestep and a spherical shape of the crystal is
 253 assumed.

254 The CN are scavenged in the model: dust particles and water ice crystals that serve as CN are captured within
 255 the formed particle, they sediment with it to lower altitudes and can be deposited on the ground. When an ice crystal
 256 sublimates, the CN (dust in case of water ice; dust, or water ice and dust in case of CO₂ ice) are released and returned
 257 to the original particle population in the grid cell.

258 2.2. MGCM

259 The MGCM is based on Forget et al. (1999), and the version we use includes the most recent advances described in,
 260 for example, Navarro et al. (2014) and Pottier et al. (2017), including water ice cloud microphysics. We do not include
 261 photochemistry in our simulations although it can have an effect on mesospheric water vapor (Navarro et al., 2014).
 262 We will discuss the possible effect of this omission in section 3.3.1.

263 The previous version of the MGCM describes CO₂ condensation with a simple parametrization and does not include
 264 an atmospheric CO₂ ice tracer (Forget et al., 1998). The parametrization of (Forget et al., 1998) treats atmospheric
 265 condensation as an instantaneous phase transition from vapor to ice when the atmosphere is supersaturated with
 266 respect to CO₂ ice ($S \geq 1$, calculated with the saturation vapor pressure of James et al. (1992)). This is followed
 267 by sedimentation throughout the atmospheric column and finally deposition at the surface of the condensed mass
 268 sedimenting from the lowest atmospheric layer. The CO₂ ice remaining in the atmosphere is re-sublimated in the end
 269 of the time step, and thus is not advected in the model. In addition to treating the atmospheric condensation in this
 270 simple way, the CO₂ condensation parametrization calculates also the direct condensation to the surface.

271 Now the new microphysics routine takes care of atmospheric condensation and sedimentation of CO₂ snow at the
 272 surface. The direct condensation at the surface and the readjustment of the atmospheric mass between model levels due
 273 to the change in the surface pressure after CO₂ condensation/evaporation are calculated as with the parametrization of
 274 Forget et al. (1998). Contrarily to the previous parametrization, the new microphysics has introduced in the MGCM
 275 an atmospheric CO₂ ice tracer, meaning that CO₂ ice is now advected by the dynamics. The atmospheric ice that
 276 sediments to the surface is incorporated into surface CO₂ ice.

277 2.3. Description of simulations

278 We have performed three simulations (see Table 1) that have been run for three Martian years. These multi-year
 279 simulations were necessary for reaching a converged state of the atmosphere (in particular of the water cycle) with the
 280 new microphysics. Initial conditions of the atmosphere are based on a previous simulation of 20 Martian years, for
 281 which a converged state of the water cycle had been reached (Navarro et al., 2014). The results have been extracted
 282 from the last (third) year of the simulations (see Table 1). The simulations had reached an overall convergence, but
 283 the total atmospheric water in the simulations showed interannual variations; this is however normal with the current
 284 version of the MGCM (see Appendix A).

285 The MGCM has been run on a 64 lon x 48 lat horizontal grid, corresponding to a spatial resolution of
 286 5.6258° longitude x 3.758° latitude, and with 32 vertical levels. The model extends from the surface to 3×10^{-3} Pa
 287 (corresponding to an approximate model top altitude of 120 km, assuming a surface pressure of 610 Pa and an
 288 atmospheric scale height of 10 km). The MGCM has been run with a dynamical time step of 1.5 minutes and a physical
 289 time step of 15 minutes. The microphysics calculations are performed 50 times per physical time step (leading to a
 290 microphysical subimestep of 18 seconds). The outputs are extracted every 2 hours. We have used the climatological
 291 dust scenario that represents the dust column optical thickness as observed during an average non-global dust storm
 292 year (Montabone et al., 2015). We do not activate the physical modules of photochemistry (Lefèvre et al., 2004;
 293 Lefèvre et al., 2008) and thermosphere (González-Galindo et al., 2009) in our simulations because of their extensive
 294 computational cost.

295 The MGCM is built in a way that allows the user to activate/deactivate some physical processes via options. Two
 296 options concern now the microphysical model of CO₂ ice cloud formation: `co2c1ouds` and `co2useh2o`. The first one
 297 is the main option of the CO₂ ice cloud microphysics. The option `co2useh2o` refers to the use of water ice particles as
 298 condensation nuclei for the formation of CO₂ clouds. The option `co2useh2o` can not be activated without activating
 299 `co2c1ouds` as well.

300 The different configurations allowed by the aforementioned options have been studied with the simulations named
 301 as follows (see also Table 1). A simulation called PARAM does not include the new CO₂ ice cloud microphysics but

Reference	co2clouds	co2useh2o	Length (MYs)	Output year
PARAM	No	No	13	3
MPCO2	Yes	No	3	3
MPCO2+H2OCN	Yes	Yes	3	3

Table 1

List of simulations performed in this study. The names of the simulations that we performed are defined in the first column. The options on the first line refer to the different configurations of the microphysical model of CO₂ ice cloud formation described in section 2.1. The option `co2clouds` indicates simulations where CO₂ ice cloud microphysics are activated, but only dust is used as CN, and `co2useh2o` refers to the use of water ice crystals, in addition to dust, as CN for the formation of CO₂ ice cloud. The length of each simulation is given in Martian Years and the output year indicates which simulation year was used for analyzing the results.

302 uses only the CO₂ condensation parametrization of Forget et al. (1998). The basic simulation with the microphysical
 303 CO₂ ice cloud formation model (option `co2clouds`) is called MPCO2. This simulation accounts only for CO₂ ice
 304 cloud formation onto mineral dust particles, ignoring water ice crystals as CN. The most realistic simulation (i.e.,
 305 accounting for as many microphysical processes as possible with the current model version) in this work is called
 306 MPCO2+H2OCN. In this simulation, the two options combined (`co2clouds` and `co2useh2o`) activate water ice
 307 crystals as CN in addition to dust for the CO₂ ice cloud formation.

308 3. Results

309 3.1. Global CO₂ ice cloud climatology

310 We will first take an overall view of the CO₂ ice cloud climatology predicted with the full microphysics by looking
 311 at the zonal and seasonal variation of the CO₂ ice column. Figure 1 shows this as a function of latitude and solar
 312 longitude for the two simulations (MPCO2, top; MPCO2+H2OCN: bottom). The figure includes also a comparison to
 313 mesospheric CO₂ ice cloud observations (black dots) from several instruments (Clancy et al., 2007; Montmessin et al.,
 314 2006, 2007; Määttänen et al., 2010; McConnochie et al., 2010; Scholten et al., 2010; Vincendon et al., 2011; Aoki et al.,
 315 2018; Clancy et al., 2019; Jiang et al., 2019; Liuzzi et al., 2021) and to the area of observed CO₂ supersaturation in the
 316 polar regions (black solid line) derived from MCS temperature profiles (Hu et al. (2012)). The two panels in Figure 1
 317 clearly demonstrate that the predicted polar winter cloud distributions are overall very similar in the two simulations,
 318 and the largest differences appear around the equator where the mesospheric clouds form.

319 Figure 1 reveals also the larger simulated latitudinal extent and a longer duration of the cloud season of the polar
 320 clouds, when compared to the extent of temperatures below CO₂ condensation derived from MCS temperature profiles
 321 (Hu et al., 2012). The column densities are also larger in the simulation MPCO2+H2OCN, meaning that more CO₂
 322 ice is condensing in the polar regions when both dust and water ice crystals are used as CN.

323 The simulation using both dust particles and water ice crystals as CN (MPCO2+H2OCN, bottom panel of Figure 1,
 324 and Figure 13) produces mesospheric clouds in a much larger seasonal range than when only dust is considered as
 325 CN (MPCO2, top panel of Figure 1). In the equatorial region, the simulation MPCO2+H2OCN is producing similar
 326 seasonal patterns as have been observed for mesospheric clouds, especially during the first half of the Martian year.
 327 However, there is a long pause in their formation around aphelion in the model, whereas cloud observations continue
 328 during this period, although they are less frequent. The long pause in cloud formation in the model is correlated with
 329 overall higher mesospheric temperatures during this period, which will be discussed in Section 3.3. The model predicts
 330 some mesospheric cloud formation at low latitudes also during the second half of the year but with very rare apparitions
 331 after $L_s = 180^\circ$. Although mesospheric cloud observations are rare in the second half of the year, some have been
 332 detected around the Southern summer solstice, and especially slightly before the Southern fall equinox, where the
 333 model also predicts cloud formation (see Section 3.3).

334 These results demonstrate that water ice crystals present in the mesosphere are necessary in our MGCM simulations
 335 to produce widespread mesospheric CO₂ ice clouds that are also more in line with the observational datasets. This
 336 reinforces the hypothesis that other CN than dust lifted from the surface participate in the formation of mesospheric
 337 clouds (Listowski et al., 2014; Plane et al., 2018). However, it should be kept in mind that our MGCM does not explicitly

Global CO₂ microphysics for Mars

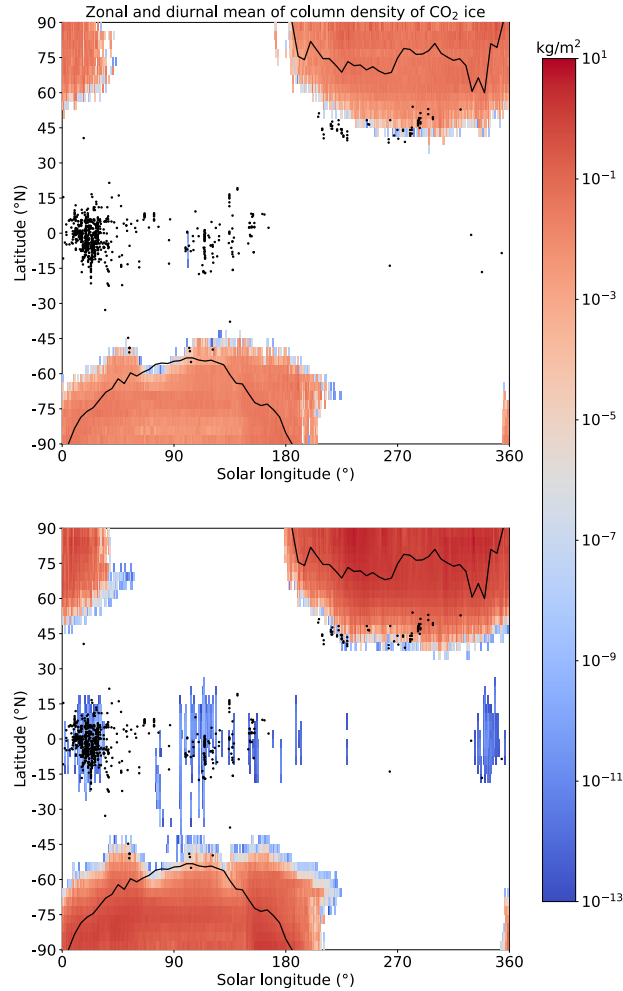


Figure 1: Zonal and diurnal mean of CO₂ ice column density (in color). Top: MPCO2 simulation; bottom: MPCO2+H2OCN simulation. The black solid line is the boundary of the area inside which MCS has observed atmospheric temperatures below the CO₂ condensation temperature (Hu et al., 2012, table 4). The black dots show available mesospheric CO₂ ice cloud observations (see text for details).

338 resolve mesoscale gravity waves (Yiğit et al., 2015) whose effect on the temperatures might be decisive in the formation
 339 of the mesospheric clouds (Spiga et al., 2012).

340 We have also looked at the frequency of CO₂ ice cloud occurrence, giving the fraction of the Martian Year
 341 when CO₂ ice clouds are present in a certain region. Figure 2 presents this fraction as a diurnal mean and with no
 342 discrimination on altitude of cloud formation nor seasonality. CO₂ ice clouds seem to form in the model at high
 343 latitudes almost all the time during the year. The polar regions host CO₂ clouds during more than half of the Martian
 344 Year, going up to ~ 70% at the South Pole. We will focus more on the polar regions in Section 3.2.1. The equatorial
 345 regions and the tropics ($\pm 30^\circ\text{N}$) see CO₂ ice clouds forming during about 10 % of the time, mainly in a zone centered
 346 at longitude -45°E . This means that equatorial mesospheric clouds preferentially form around this longitude in the
 347 model. There are also other zones in the southern tropics that have similar cloud formation frequencies. Observations
 348 have shown that the equatorial mesospheric clouds seem to cluster in certain longitudinal corridors (Määttänen et al.,
 349 2013), one of which roughly corresponds to the occurrence maximum seen here. The other longitudes where tropical
 350 cloud formation is predicted are quite close to some of the longitudinal corridors where cloud formation has been
 351 observed ($\pm 180^\circ\text{E}$). The feature around -45°E is discussed more in detail in Section 3.3 where we focus on the results
 352 on mesospheric clouds.

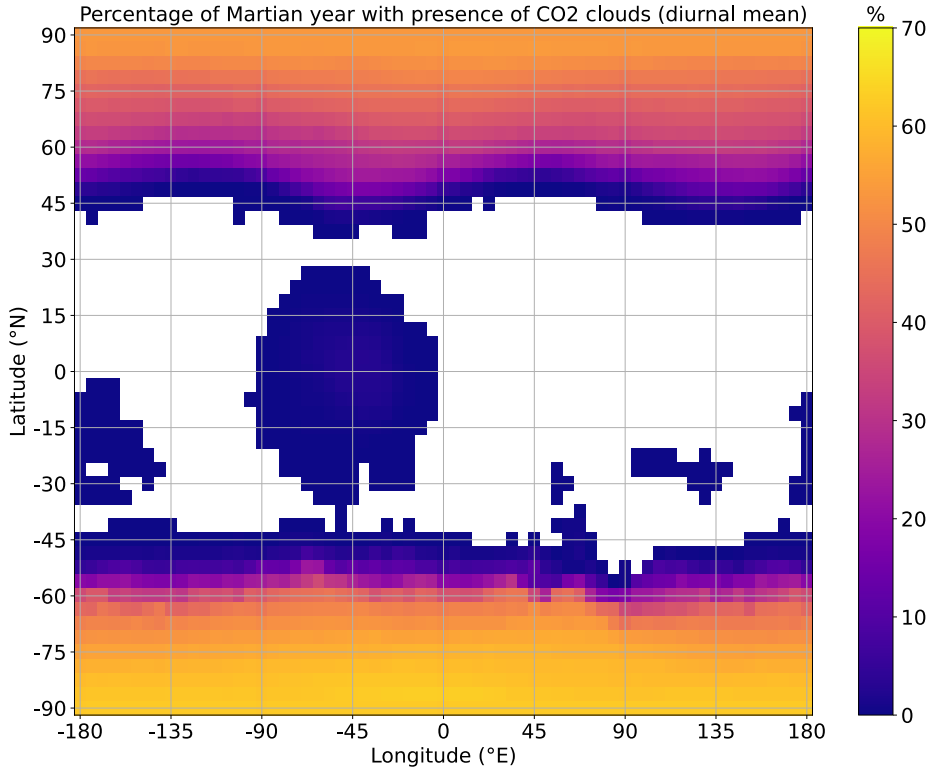


Figure 2: Fraction (in percent) of a Martian Year with CO₂ ice cloud occurrence as a diurnal mean in the MPCO2+H2OCN simulation.

3.2. Polar regions

3.2.1. Polar CO₂ ice clouds

First of all we look at the thermal structure of the polar atmosphere. Hu et al. (2012) used MCS data to infer the thickness of the supersaturated near-surface layer in the polar nights. We have extracted the same parameter from the simulation MPCO2+H2OCN and we compare it to the MCS data of Hu et al. (2012) in Figure 3. The MCS data are from MY 29 whereas our simulation uses the climatological dust distribution. MY 29 was a year devoid of global dust storms, but dust activity especially during the latter half of the year might differ somewhat from the climatology dust scenario.

In the northern polar region, the modeled supersaturated layer is on average thicker (15-20 km) than the observed one (5-12 km), but the modeled variability (shown by the error bars) is large and the variabilities of the layer thickness overlap for most of the time. Supersaturated layers are also predicted during a longer period than what the observations revealed, starting a bit earlier (around $L_s = 180^\circ$) and lasting up to $L_s = 30^\circ$. Thus, the model seems to predict an overall colder polar atmosphere than what the observations show.

In the Southern polar regions the supersaturated layer thicknesses show a similar seasonal variability but the modeled layer thickness is larger by a factor of 1.5-2 than the observed ones throughout the winter; The seasonal duration of the supersaturated layer is in the south more in line with the observed duration of polar supersaturation, with only a slightly earlier start and later end of the supersaturated period.

As the modeled supersaturated layers in the polar regions are often thicker than the ones seen in observations, we expect the clouds to extend to higher altitudes as well. This can be seen by comparing the simulated clouds to the observed MOLA cloud tops (Fig. 4). The cloud top altitude equivalent to what MOLA observed can be calculated following the approach of Pettengill and Ford (2000). The MOLA laser was backscattered when the integrated optical thickness of a cloud reached a certain level, depending on the number concentration of the particles and the crystal radius. The threshold crystal number concentration N_{refl} (in m^{-3}) is calculated as a function of the crystal radius (in μm) with the equation $N_{\text{refl}} = 2 \cdot 10^{-8} r^{-2}$. Going from higher altitudes towards the surface (just like the lidar beam),

Global CO₂ microphysics for Mars

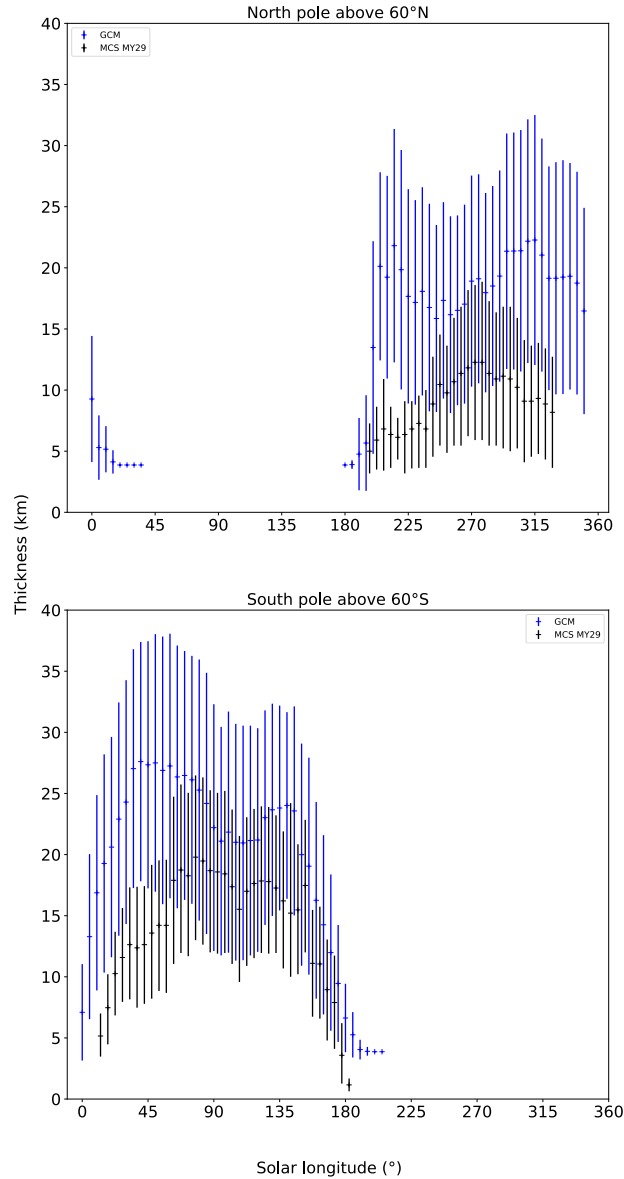


Figure 3: Thickness (blue crosses) and variability (standard deviation, blue error bars) of the supersaturated layer at the poles in the simulation MPCO₂+H₂OCN below 70 km altitude, compared with MCS data from MY 29 (black crosses and error bars), extracted from Figure 9 of Hu et al. (2012). Top panel: North pole (60-90°N), bottom panel: South pole (60-90°S).

377 this threshold value is compared to the modeled crystal number concentration and the backscattering level is the level
 378 where this value is reached or exceeded. The panels of Figure 4 show this comparison. MOLA polar cloud tops (bottom
 379 panel) were generally below 10 km altitude with occasional cloud tops observed between 10 and 15 km. The modeled
 380 MOLA-equivalent cloud tops (top panel), calculated from the given equation, reach much higher altitudes, exceeding 10
 381 km and reaching well above 20 km in most of the polar regions. Already the previously discussed thicker supersaturated
 382 layer may fully explain these differences, but an additional explanation to the discrepancy might come from the large
 383 particle sizes our model predicts in the polar regions, reaching values of some 10s of μm . As the threshold number
 384 concentration is inversely proportional to the square of the crystal radius, these large radii cause the threshold to be
 385 low and thus it is reached at higher altitudes than in the case of smaller radii. In addition, Pettengill and Ford (2000)

Global CO₂ microphysics for Mars

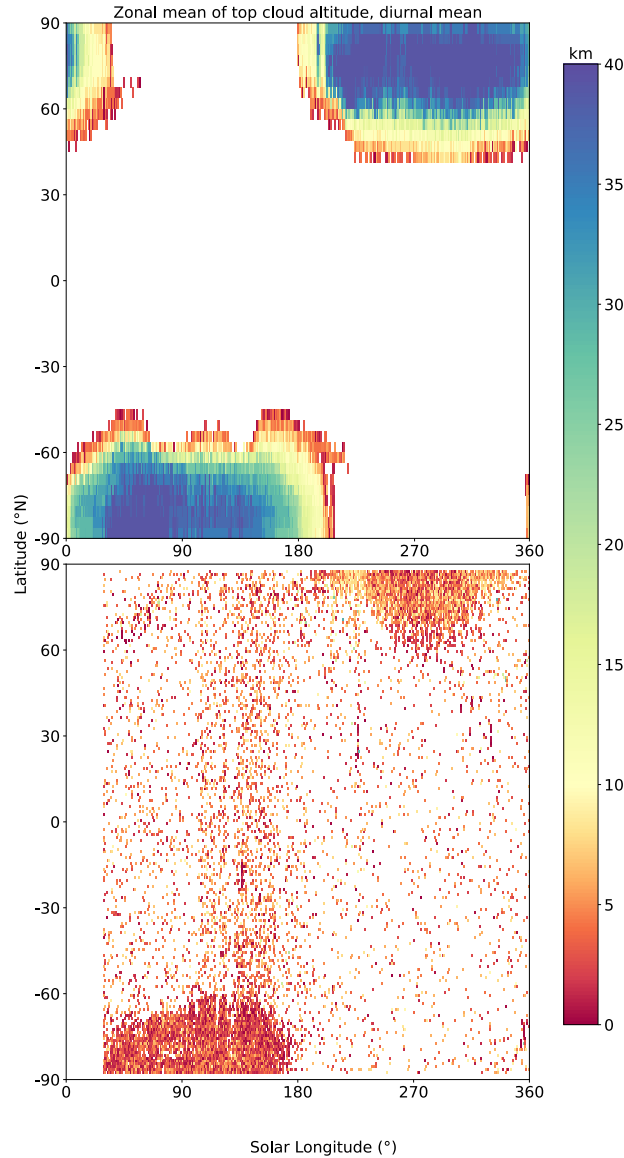


Figure 4: Zonal mean of CO₂ ice cloud top altitudes in the polar regions. Top: Cloud tops in MPCO₂+H₂OCN simulation as should be seen by MOLA when applying the approach of Pettengill and Ford (2000); bottom: Cloud top altitudes from MOLA observations (Neumann et al., 2003) averaged in a 1° × 1° grid.

386 supposed in their approach a nominal radius of 1 μm , whereas our crystals are an order of magnitude larger (see also
387 Figure 7).

388 We can also see in Figure 4 that the clouds reach lower latitudes in the simulation, extending to 45° latitude in both
389 hemispheres. The vertical, seasonal and spatial distribution of the modeled polar clouds lead us to conclude that the
390 modeled polar atmosphere is colder than it should be. This might be explained by an excess of dust in the polar night in
391 the model compared to reality. Although the dust profile can evolve freely in the model, the MGCM total dust column
392 is forced by scenarios based on observations (Montabone et al., 2015); nevertheless, in the dust scenarios there is a
393 lack of observations in the polar regions, in which case the dust column is fixed to a minimum value (Montabone et al.,
394 2015). This value might be too large for the polar night, causing an excessive radiative cooling of the polar regions and
395 too cold polar winter temperatures. This problem will be explored in dedicated future studies.

Global CO₂ microphysics for Mars

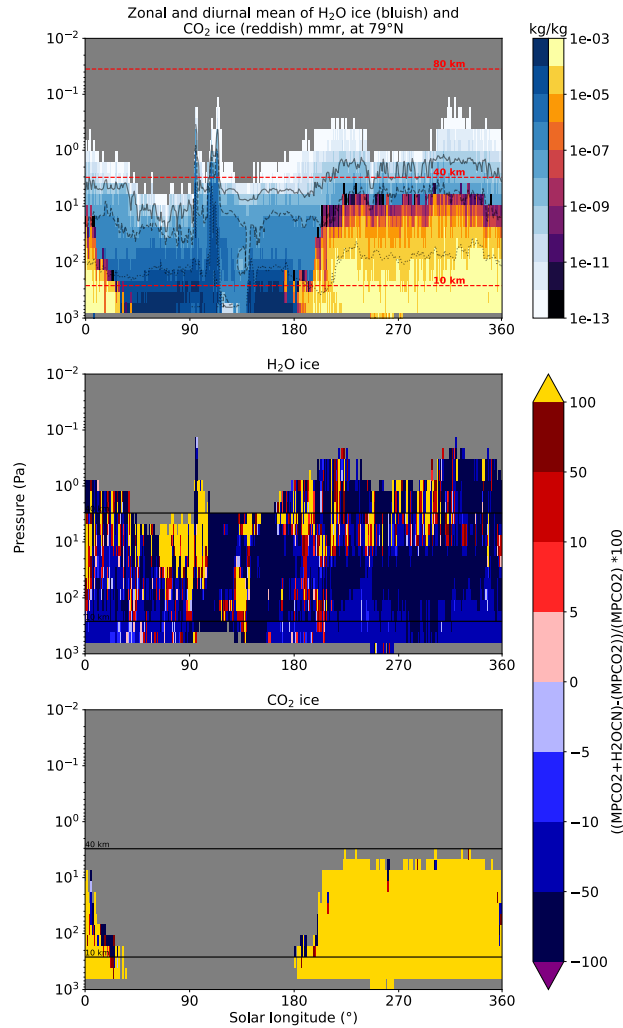


Figure 5: The zonal and diurnal mean of water ice (red-yellow color table) and CO₂ ice (blue color table) mass mixing ratios as a function of season and altitude (pressure) in the Northern polar region (79°N). Top: MPCO2 simulation; middle: water ice mass mixing ratio relative difference (%) between the simulations MPCO2+H2OCN and MPCO2; bottom: CO₂ ice mixing ratio relative difference. The horizontal lines give an indication of the corresponding altitudes above the surface. The contour levels in the top panel refer to H₂O ice mass mixing ratios of 10⁻⁹ (solid line), 10⁻⁷ (dashed line) and 10⁻⁵ (dotted line).

396 We can still take a closer look at the polar regions through vertical cross-sections of zonal mean H₂O and CO₂
 397 ice mixing ratios as a function of season for both the MPCO2 and the difference of MPCO2+H2OCN and MPCO2
 398 simulations (Figure 5 for 79°N and Fig. 6 for 79°S). In these figures it is clearly visible that water ice clouds persist
 399 in the polar regions throughout the year, whereas CO₂ ice clouds are limited to the polar winter season. Comparing to
 400 MCS observations of the polar hoods (Benson et al., 2010, 2011) that showed clouds extending up to 40 km at both
 401 poles, it appears that in the Northern polar regions also the modeled water ice clouds extend to higher altitudes than
 402 what has been observed (Benson et al., 2011). At the north pole, the CO₂ ice mass mixing ratios of the order of 100s
 403 to 1000s of ppm shown in Figure 5 are consistent with the results of Kuroda et al. (2013) who compared their CO₂
 404 ice cloud parameterization output to MCS observations in the northern polar region. The difference plots show how
 405 the water ice cloud distribution changes between the two simulations (middle panels of Figures 5 and 6). Water ice
 406 depletion is seen where CO₂ ice forms: this is due to the water ice crystals acting as CN for CO₂ ice. When water ice

Global CO₂ microphysics for Mars

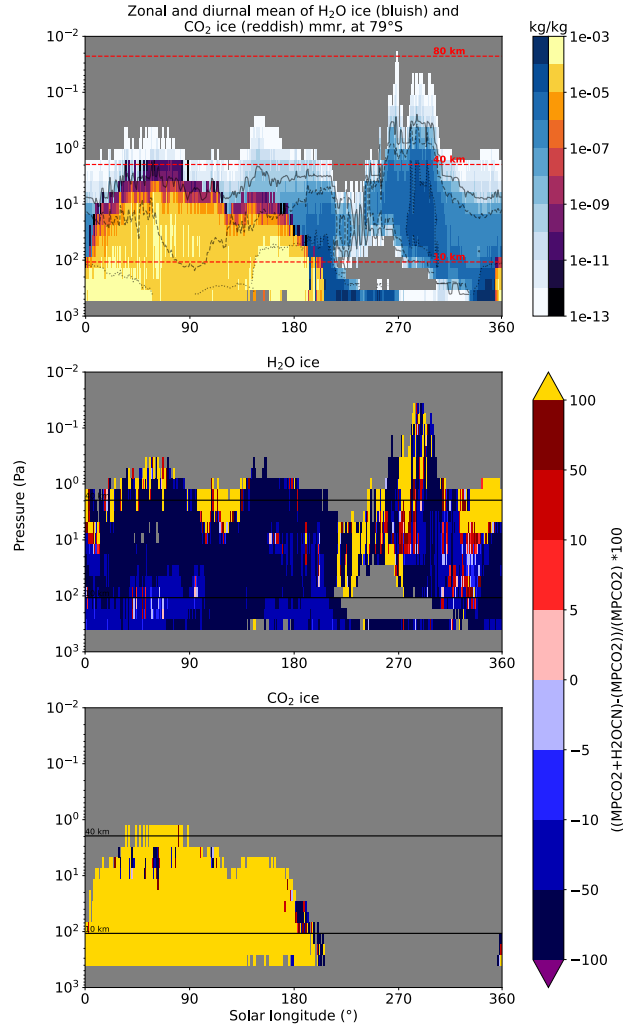


Figure 6: Same as Figure 5 but for the Southern polar regions (79°S).

407 crystals are used as CN as well, there is a clear increase in the CO₂ ice mixing ratio, shown by the increase in CO₂ ice
 408 at all altitudes where CO₂ ice clouds form in the lower panels of Figures 5 and 6.

409 The particle radii (Fig. 7) go up to and slightly above 10 μm on average near the surface with a large variability.
 410 A clear latitudinal trend (colors: see legend) is also visible in Figure 7, with the largest particles modeled at the pole
 411 and the smallest ones at the lowest latitudes (60°). The crystal radii are anyhow between 1 and 10 μm near the surface,
 412 with these sizes persisting to fairly high altitudes (10 Pa). In the northern polar region the mean radii remain above
 413 1 μm up to 10 Pa at almost all latitudes and decrease below this value only at the top of the clouds. In the southern
 414 polar regions, there is a more distinct trend with a steeper decrease with altitude of the particle radii, and in the lowest
 415 latitudes (60°S-70°S) the crystal sizes fall below 1 μm very rapidly with increasing altitude (20-100 Pa). Looking at
 416 the difference between the MPCO₂ and MPCO₂+H₂OCN simulations, shown in the rightmost panels of Fig. 7, we
 417 can see that the crystal radii decrease by up to 100 μm at all altitudes in both hemispheres in the MPCO₂+H₂OCN
 418 simulation that also accounts for the water ice crystals as CN. This decrease is likely related to the larger number of
 419 available CN that consequently leads to smaller CO₂ crystal sizes in the MPCO₂+H₂OCN simulation.

420 Particle sizes are difficult to measure in the polar night. An indirect estimate of an average particle size over the
 421 poles by Hu et al. (2012) from seasonal polar cap mass estimates combined with a calculation of the atmospheric
 422 condensed and sedimented mass indicated particle radii of 8–23 μm in the north and 4–13 μm in the south. Also
 423 Hayne et al. (2012, 2014) derived a size range of 10-100 μm for CO₂ ice crystals from MCS observations. Modeling

Global CO₂ microphysics for Mars

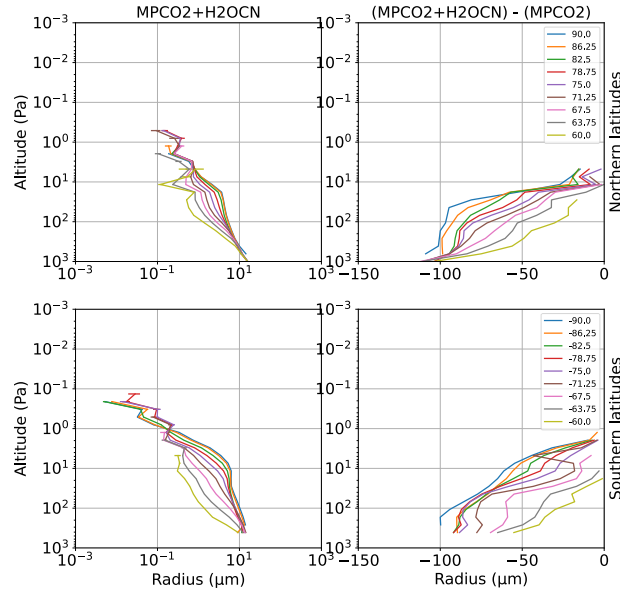


Figure 7: Left: Zonal, annual and diurnal mean CO₂ ice radius profiles (in μm) in the polar regions for MPCO₂+H₂OCN simulation for a given latitude, given by the color code as shown in the legend. Right: the difference (in μm) in crystal radii between MPCO₂+H₂OCN and MPCO₂ simulations. Top: north polar region; bottom: south polar region.

424 has provided more estimates on the particle sizes in the polar clouds. Tobie et al. (2003) modeled clouds forming below
 425 15 km with particle sizes going from $<10 \mu\text{m}$ up to several tens of micrometers. The maximum radii depended on the
 426 assumptions of their model, such as the number of CN or the critical saturation ratio required for nucleation. Colaprete
 427 and Toon (2002) and Colaprete et al. (2003, 2008) performed several CO₂ ice cloud modeling studies, some of which
 428 focused on the polar regions. Colaprete and Toon (2002) modeled carbon dioxide snow storms in the polar regions with
 429 particle effective radii reaching several hundreds of micrometers (up to $> 400 \mu\text{m}$), and convective cloud simulations
 430 at the south pole resulted in radii between 50 and $200 \mu\text{m}$ (Colaprete et al., 2003). Global simulations by Colaprete
 431 et al. (2008) predicted crystals of $100 \mu\text{m}$ average radii in the polar regions, varying from some tens of microns to
 432 more than $200 \mu\text{m}$.

433 The particle sizes modeled in this work are at the lower end of the range estimated from observations and there
 434 may be several reasons for this. A GCM can not resolve subgrid scale processes such as convection that could result in
 435 larger crystal sizes (Colaprete et al., 2003). The water cycle of the MGCM produces thicker polar water ice clouds than
 436 has been observed (Navarro et al., 2014) and thus the amount of water ice CN might be overestimated by the model.

437 3.2.2. Surface CO₂ ice

438 We have also looked at the amount of CO₂ ice forming the polar ice caps on the surface. Snowfall from clouds can
 439 contribute to the formation of the surface ice, but it is not straightforward to estimate from observations the relative
 440 contributions to the surface ice of direct condensation and snowfall. We can now perform such an estimation using
 441 model simulations and in addition we can compare the surface ice extent predicted by the simple CO₂ condensation
 442 parametrization and the full microphysics.

443 Figure 8 shows surface fluxes of direct CO₂ condensation and CO₂ snowfall in the simulation MPCO₂+H₂OCN
 444 averaged over the 60-90° latitude band in the northern (top panel) and southern (bottom panel) polar regions as a
 445 function of solar longitude. The snowfall flux is at its maximum of the order of 10% of the total flux in the north
 446 during the whole winter. In the south, the flux reaches a similar relative value of 10% of the total flux in the fall and
 447 in the spring, and is smaller during the rest of the winter. Snowfall also continues on both hemispheres even when the
 448 surface ice cap is already sublimating, which could be explained by episodic snow storms (hinted to by the variability
 449 of the flux at these seasons) above the sublimating cap. In the northern hemisphere snowfall starts around the same time
 450 ($L_s = 180^\circ$) as direct condensation, but in the South direct condensation has already started before snowfall appears

Global CO₂ microphysics for Mars

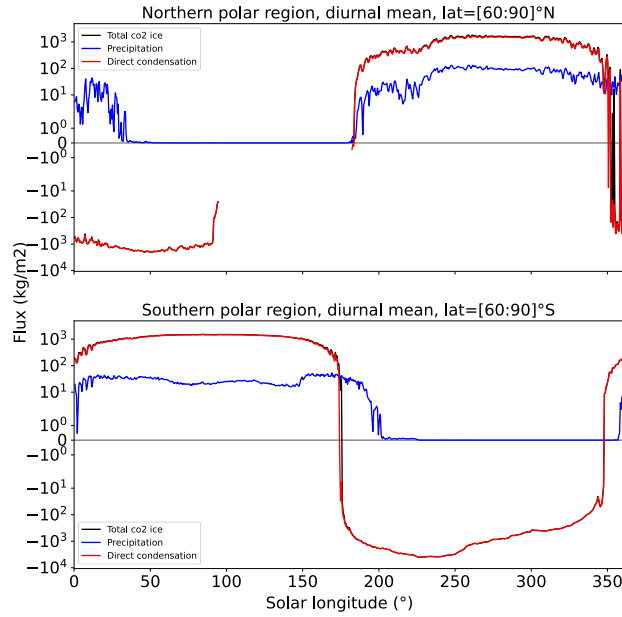


Figure 8: Seasonal variation of the zonal (and diurnal) mean of the CO₂ direct condensation (red) and snowfall (blue) fluxes, and their sum (black) over the polar regions (60-90° latitude) in the north (top panel) and in the south (bottom panel).

451 (around and after $L_s = 350^\circ$). Here we will not investigate in detail the dynamics of the polar hood as we will focus
 452 on the polar regions in a future study.

453 Figure 9 displays the surface CO₂ ice in the PARAM simulation (without CO₂ ice cloud microphysics) over 12
 454 Martian "months" of 30° of solar longitude each. This simulation models the formation of the surface ice by direct
 455 condensation and a contribution coming from sedimentation of atmospheric ice via a simple parametrization, as
 456 described in Section 2.2.

457 Figure 10 shows the difference in percent of surface CO₂ ice in the MPCO2+H2OCN simulation and in the PARAM
 458 simulation over the same 12 Martian "months", revealing the influence the realistic CO₂ ice cloud microphysics has on
 459 the surface ice distribution. This influence can be direct through snowfall or indirect through, for example, scavenging
 460 of dust and water ice crystals whose radiative effects would then be consequently diminished. One might expect the
 461 influence of microphysics to be negligible, but as it can be seen in the top panel of Figure 10, the surface ice displays
 462 large, both positive and negative changes in the full microphysics simulation in the majority of the northern polar
 463 region throughout the winter. Similarly, in the south there are patchy, persistent patterns of increased and decreased
 464 surface ice.

465 In some regions (for example, longitudes 0 – 90°E and 270 – 360°E in the north, and longitudes 0 – 90°E and
 466 180 – 300°E in the south in Fig. 10), the patterns of increased surface ice with microphysics are quite stationary from
 467 one month to another. These patterns do not seem correlated with cloud features shown in Fig. 11. In the seasons
 468 $L_s = 60 - 120^\circ$ in the north and $L_s = 240 - 330^\circ$ in the south, no clouds are predicted by the model (see Fig. 1), but
 469 there are changes in the surface ice in the microphysics simulation compared to the parameterized one. We interpret the
 470 larger surface ice mass in some regions during these periods as a result of an overall larger surface ice mass accumulated
 471 during the winter that takes a longer time to sublimate during summer. Indeed, as can be seen in Fig. 8, both in the
 472 south and in the north, snowfall lasts quite a long time in the MPCO2+H2OCN simulation after the direct sublimation
 473 has started, thus maintaining a positive surface ice budget for a longer time.

474 The underlying reason for an increase in surface ice mass in the simulation accounting for microphysics is probably
 475 due to the fact that the microphysics code (simulations MPCO2 and MPCO2+H2OCN) allows for the formation
 476 of supersaturation, whereas the simple parametrization previously used in the model (simulation PARAM) induces
 477 an immediate condensation at saturation. Supersaturations attained at the poles have been measured to be around
 478 20% to 30 % on average (Hu et al., 2012) and heterogeneous nucleation can start already at saturation ratios of the

Global CO₂ microphysics for Mars

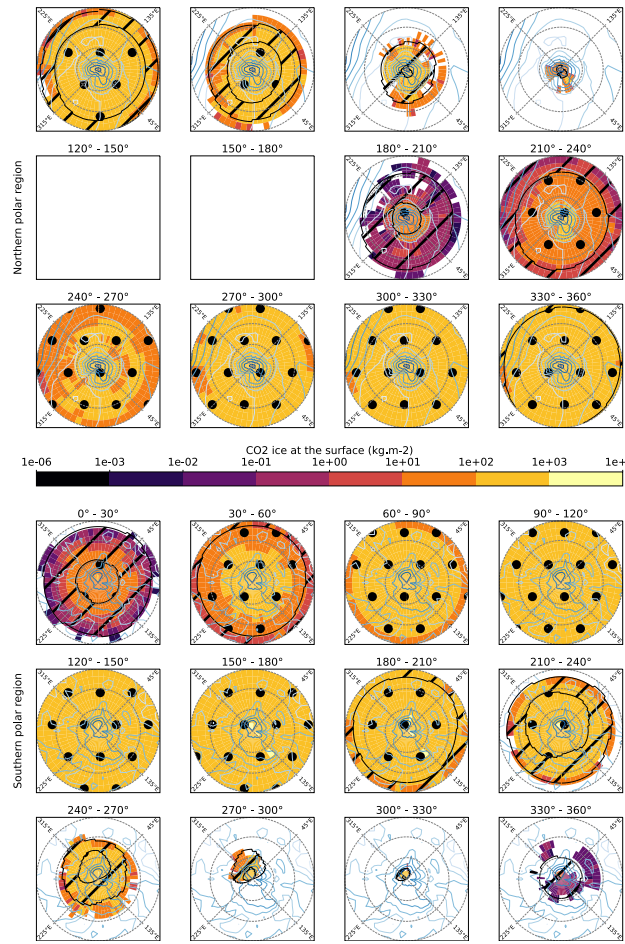


Figure 9: Polar projection of CO₂ ice at the surface for PARAM simulation (diurnal mean) for 12 Martian "months" of 30° of L_s each for the North pole (top) and the South pole (bottom). Bluish contour plot refers to martian topography. Polar CO₂ ice caps from TES data (Titus, 2005) are represented by hatched areas: the dotted zones refer to permanent ice during the L_s period, the stripes refer to the zones inside which the ice boundaries extend during the L_s period. In plots for the northern polar region, the longitude 0°E is located at the bottom on each subplot; in the southern polar region, it is located at the top.

479 order of $S > 1.35$ (Glandorf et al., 2002), which is higher than unity. Thus, using detailed microphysics (simulation
 480 MPCO2+H2OCN) leads to a larger amount of vapor available for condensation, and thus a larger condensed mass
 481 available in the atmosphere that can subsequently be deposited at the surface. Naturally, only condensing more mass in
 482 the atmosphere does not necessarily lead to larger snowfall, which depends on the particle size as well. As can be seen
 483 in Figure 7, the crystal radii attain values of about 10 micrometers, leading to sedimentation velocities of the order of
 484 0.1 m/s. This implies that the crystals can fall to the ground from the first 5 km of the atmosphere in less than a day.

485 However, the heterogeneity of the increase/decrease patterns of surface ice can not be explained with the increased
 486 cloud cover only, but probably some atmospheric dynamics are playing a role in determining where snowfall and thus
 487 surface ice increase. Kuroda et al. (2013) investigated the baroclinic activity around the north pole and revealed that
 488 the CO₂ ice clouds occurred within the cold phases of such waves. We are showing in Fig. 12 a similar investigation as
 489 in Fig. 2 (upper panel) of Kuroda et al. (2013) to reveal the effect of waves that are averaged out in our monthly plots of
 490 Fig. 11. Fig. 12 shows a very similar behavior of the waves as in Kuroda et al. (2013) with the waves moving east with
 491 time. Their warmest phases are found in the western and eastern hemispheres, with the CO₂ ice clouds forming in the
 492 cold phases of the waves. In our model, the wave amplitudes are the largest in the beginning of the studied period and
 493 they decrease clearly towards the end of the period: such a weakening of the waves is not seen in the results of Kuroda

Global CO₂ microphysics for Mars

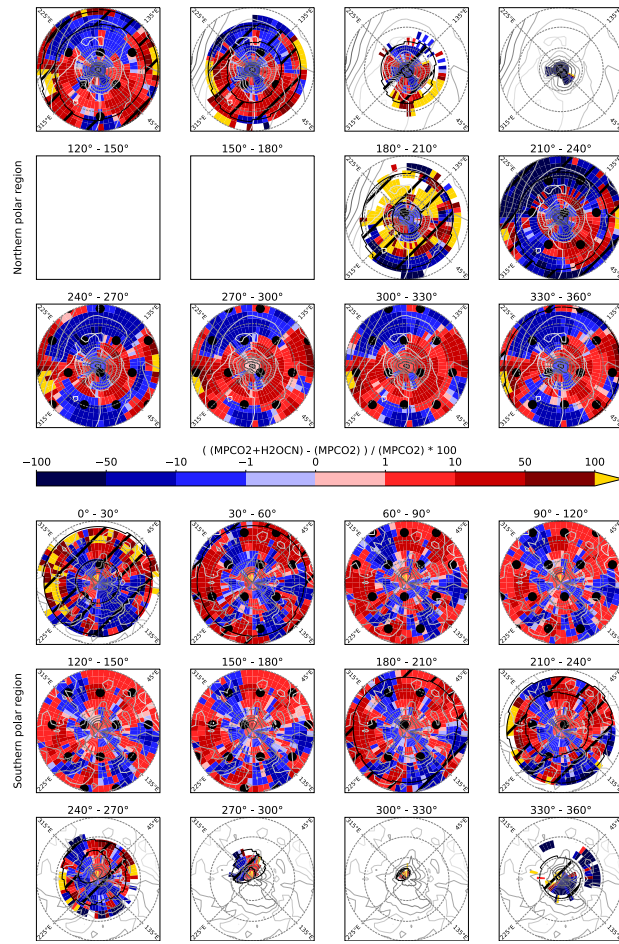


Figure 10: Polar projections for 12 Martian "months" of 30° of L_s each of the relative difference in surface CO₂ ice (in %) between MPCO₂+H₂OCN and PARAM simulations for the North pole (top) and the South pole (bottom). Grey contour plot refers to martian topography. Polar CO₂ ice caps from TES data (Titus, 2005) are represented by hatched areas: the dotted zones refer to permanent ice during the L_s period, the stripes refer to the zones inside which the ice boundaries extend during the L_s period. In plots for the northern polar region, the longitude 0°E is located at the bottom on each subplot; in the southern polar region, it is located at the top.

494 et al. (2013). Due to the colder temperatures found in our model, CO₂ ice cloud formation is clearly increased especially
 495 after $L_s = 290^{\text{circ}}$. If we compare the preferred longitudes of CO₂ ice cloud formation in Fig 12 and the differences in
 496 surface CO₂ ice mass in Fig. 10), the waves may at least partly explain the longitudinal patterns of increased CO₂ ice
 497 mass.

498 On Figures 9 and 10, we have also plotted the polar CO₂ ice caps from TES data (Titus, 2005): dotted areas refer
 499 to 100% ice cover during the L_s period, hatched areas refer to the area in which the ice extended during the L_s period.
 500 The CO₂ ice simulated at the surface is in good agreement with TES observations for both polar regions. The behavior
 501 of CO₂ ice sublimation in the southern polar region is in line also with TES observation between $L_s = 270^\circ$ - 330° .
 502 But, simulations also show CO₂ ice deposits earlier than TES observations in the southern polar region between $L_s =$
 503 330° - 360° , and longer in the northern polar region between $L_s = 90^\circ$ - 120° .

504 3.3. Mesospheric CO₂ ice clouds

505 Subcondensation temperatures and mesospheric clouds have been observed at the equator, in the tropics and at
 506 midlatitudes (see, for example, Forget et al., 2009; Hu et al., 2012; Montmessin et al., 2006; Clancy et al., 2007;
 507 Montmessin et al., 2007; Määttänen et al., 2010; Scholten et al., 2010; McConnochie et al., 2010; Aoki et al., 2018;
 508 Clancy et al., 2019; Jiang et al., 2019). Supercold pockets observed by MCS were found between 0.1 and 1 Pa (Hu

Global CO₂ microphysics for Mars

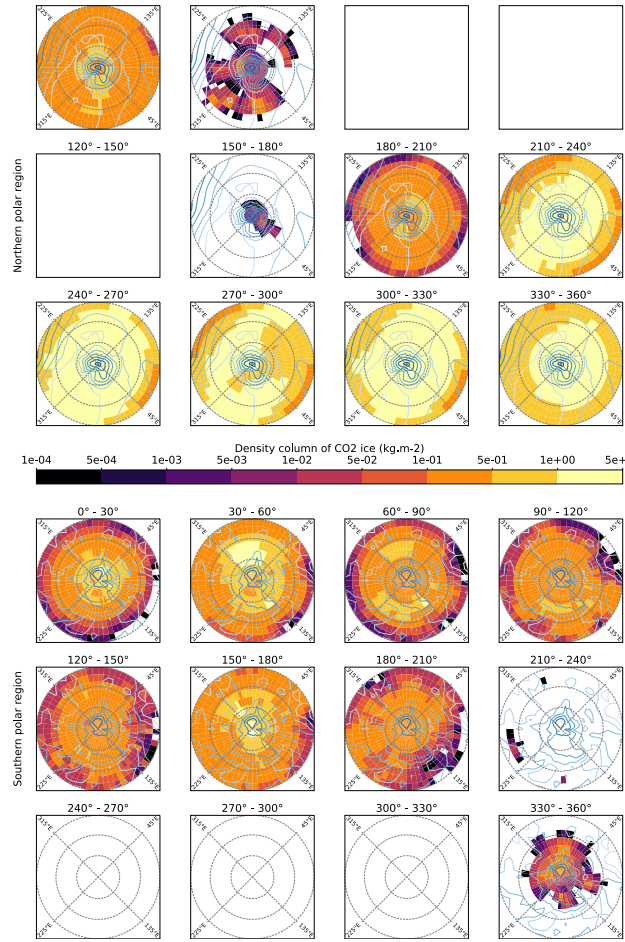


Figure 11: Polar projection of atmospheric CO₂ ice column for MPCO2+H2OCN simulation (diurnal mean) for 12 Martian "months" of 30° of L_s each for the North pole (top) and the South pole (bottom). Grey contour plot refers to martian topography. In plots for the northern polar region, the longitude 0°E is located at the bottom on each subplot; in the southern polar region, it is located at the top.

509 et al., 2012), whereas SPICAM observed temperature minima within such pockets around 0.001 Pa, corresponding to
 510 approximately 100 km (Forget et al., 2009). It should be noted that the observed altitude ranges and local times are
 511 different for the two instruments: MCS observes only twice a day (3 AM and 3 PM) going up to about 80 km and
 512 SPICAM profiles come from nighttime stellar occultations reaching to 120-130 km. These observations confirmed
 513 that the mesosphere can be supersaturated with respect to CO₂ ice in a large range of altitudes. Similarly, the CO₂
 514 ice cloud observations (e.g., Montmessin et al., 2006; Clancy et al., 2007; Montmessin et al., 2007; Määttänen et al.,
 515 2010; Scholten et al., 2010; McConnochie et al., 2010; Aoki et al., 2018; Clancy et al., 2019) are spread over an altitude
 516 range going from 50 to 100 km, depending on the instrument and particularly on the local time of the observations that
 517 spans from early in the morning (7-11 AM local time) to midnight, with the majority of the observations being in the
 518 afternoon.

519 In this section we focus on the predicted mesospheric CO₂ ice clouds and compare them to the published
 520 observations.

521 3.3.1. Effect of water ice condensation nuclei

522 The top panel of Figure 1 showed that the simulation with cloud crystals forming only onto dust particles
 523 (simulation MPCO2) formed very few equatorial/tropical clouds in a very short seasonal range right after the northern
 524 summer solstice. One of the reasons for this could be that the temperatures in the MGCM are too high in the mesosphere

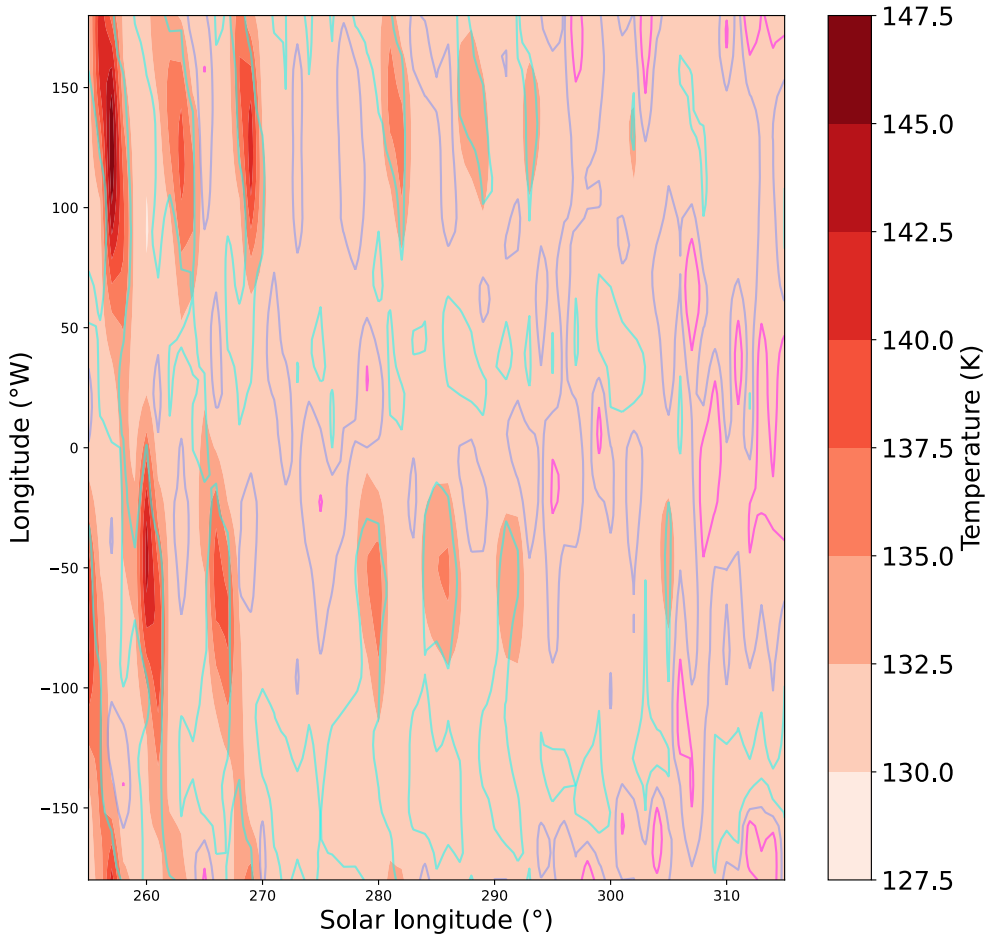


Figure 12: Solar longitude-longitude Hovmöller plot for $L_s = 255 - 315^\circ$ at 80°N and at 50 Pa pressure level of temperature (colors) and CO₂ ice mass mixing ratio (contours) in the simulation MPCO₂+H₂OCN. The CO₂ ice contours correspond to the following mass mixing ratio values: cyan: 10^{-3} ; blue: 5×10^{-3} ; magenta: 10^{-2} . This plot is similar to Fig. 2 of Kuroda et al. (2013).

525 (González-Galindo et al., 2011). Another likely reason, as shown by Listowski et al. (2014), is that the small amounts
 526 of dust particles that have very small radii (as the larger ones fall out rapidly) are insufficient as CN to initiate cloud
 527 formation that would lead to an observed-like cloud distribution. As water ice crystals can form at higher temperatures
 528 than CO₂ ice, it is likely that water ice crystals are present prior to CO₂ condensation in the Martian atmosphere. This
 529 was the motivation for including in our model the capacity to use H₂O crystals as CN for CO₂ ice cloud formation
 530 (simulation MPCO₂+H₂OCN). The bottom panel of Figure 1, based on the results of the MPCO₂+H₂OCN simulation,
 531 shows that including water ice crystals as CN significantly increases the amount of mesospheric CO₂ ice clouds (their
 532 column densities), and that they form at seasons corresponding to the observations in the tropics and at some seasons
 533 also at midlatitudes, especially around $L_s = 80-120^\circ$. Navarro et al. (2014) showed that the MGCM was capable of
 534 reproducing the presence of supersaturated water vapor (in quantities of less than a ppmv) at high altitudes, and here
 535 we see that even such small amounts water vapor and water ice can have measurable consequences in the middle
 536 atmosphere.

537 However, it should be noted here that we do not account for photochemistry in our simulations. Navarro
 538 et al. (2014) discussed the importance of photochemistry on mesospheric water vapor supersaturations, saying that
 539 photodissociation could not be neglected for the large mesospheric supersaturations they encountered, but they did
 540 not quantify its effect on water vapor concentrations nor ice formation in the mesosphere. Our simulations are
 541 computationally expensive with both water ice and CO₂ ice cloud microphysics activated, so we have not included

Global CO₂ microphysics for Mars

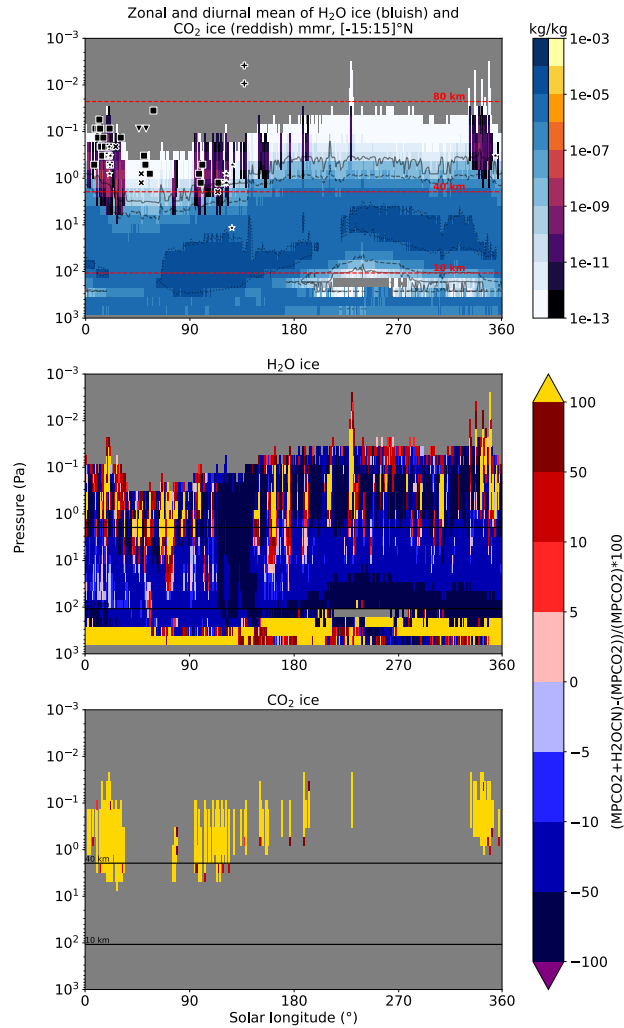


Figure 13: Top panel: Seasonal evolution of the vertical distribution of the zonal and diurnal mean H₂O ice mass mixing ratio (blue color table) and CO₂ ice mass mixing ratio (red-yellow color table) between 15°S and 15°N, for the MPCO₂+H₂OCN simulation. Observational data (in black): square = HRSC, triangle = OMEGA nadir, crosses = SPICAM, X = THEMIS, stars = NOMAD. The contour levels in the top panel refer to H₂O ice mmr at 10⁻⁹ (solid line), 10⁻⁷ (dashed line), and 10⁻⁵ (dotted line). Middle panel: The relative difference (%) in water ice mass mixing ratio between the simulations MPCO₂+H₂OCN and MPCO₂. Bottom panel: The relative difference (%) in CO₂ ice mass mixing ratio between the simulations MPCO₂+H₂OCN and MPCO₂. The horizontal lines give an indication of the corresponding altitude above the surface.

542 photochemistry in these first simulations. This is not the only process that we have for the moment overlooked, and
 543 future simulations with a further improved model (including CO₂ ice cloud radiative effects, meteoric particle CN, etc.)
 544 will also take into account photochemistry and thermospheric processes. We have benefited from recent simulations
 545 looking into the HDO cycle (Vals et al., 2022) that were also used for testing the effect of photochemistry on the
 546 water cycle. These simulations did not include CO₂ ice cloud microphysics. According to the simulations of Vals et al.
 547 (2022), including photochemistry reduces the volume mixing ratio of water vapor in the middle atmosphere. However,
 548 the effect of photochemistry on water ice is less straightforward, as ice formation does not only depend on vapor
 549 concentration but is a strong function of the temperature and thus very sensitive to dynamic and radiative effects. In
 550 an attempt to estimate the perturbation on water ice amount by the formation of CO₂ ice clouds, we have looked at the
 551 relative difference in water ice between simulations MPCO₂+H₂OCN and MPCO₂ in the equatorial mesosphere (see
 552 middle panel of Fig. 13). The relative differences of the tiny water ice mass mixing ratios can be large (up to 100%), but

the water ice field does not seem to change significantly due to CO₂ ice cloud formation: the variations in water ice are of smaller temporal and vertical scale than those of CO₂ ice cloud formation and are not directly correlated. This leads us to the same conclusion as above after the discussion on photochemistry in the results of Vals et al. (2022): CO₂ ice cloud formation seems to have a lesser effect on the variations in water ice concentrations than other (dynamical and radiative) processes. We acknowledge that this can only be verified and quantified with dedicated simulations that we will perform in a future study.

Fig. 13 reveals the cloud formation at the equatorial region in detail through a vertical cross-section of the zonal and diurnal mean H₂O and CO₂ ice mixing ratios over a Martian Year. What can be seen is that the CO₂ ice clouds form at the top of the water ice cloud layer whose seasonal altitude variation they follow, the CO₂ ice clouds forming approximately between ~ 30 and 0.1 Pa (up to 0.004 Pa).

It should be mentioned here that although a quantitative comparison with observations is difficult, qualitatively the behavior of the modeled water ice clouds, especially their seasonal altitude variations, is consistent with observations (Clancy et al., 2019).

The model of Colaprete et al. (2008) predicted CO₂ ice clouds forming between 10 to 1 Pa, but their model top was lower (80 km), inhibiting the modeling of higher altitude clouds. The seasonality of equatorial mesospheric CO₂ clouds in the model of Colaprete et al. (2008) does not correspond to the observed one, as their model formed clouds mainly after $L_s = 150^\circ$. CO₂ ice cloud formation in our model is in good agreement with observational data from HRSC, THEMIS and NOMAD, except that there is a clear pause in predicted cloud formation in the model between $L_s=40-80^\circ$, whereas the observations shown in Fig. 13 seem to have a pause starting slightly later on ($L_s=60-100^\circ$). CO₂ ice clouds observed by OMEGA (in nadir view) and SPICAM are higher in altitude than our simulated CO₂ ice clouds, likely due to a lack of CN and warmer temperatures that prevent CO₂ ice cloud formation. In our simulations, the temperature structures (not shown) between the simulations MPCO2 (dust only as CN) and MPCO2+H2OCN are not different. The only difference is the additional source of CN on the latter simulation. This provides us enough clues to conclude that the increase in CO₂ ice clouds in the MPCO2+H2OCN simulation compared to MPCO2 is solely due to this source of CN. However, just like in the 1D simulations with mineral dust only as CN of Listowski et al. (2014), the optical thickness τ of these mesospheric CO₂ ice clouds (Fig. 14) is several orders of magnitude below unity (observed maximum τ of daytime CO₂ ice clouds, Montmessin et al., 2007; Määttä et al., 2010). The optical thickness in the model remains also lower than the moderate τ values of some tenths observed by Clancy et al. (2019). This points towards a need for a more abundant, exogenous CN source, postulated already by Listowski et al. (2014) and suggested to be icy metal carbonate nanoparticles formed as a result of meteor ablation (Plane et al., 2018). We are including such a CN source in our model and will explore its effect in a future publication.

3.3.2. Temporal and meridional distribution of mesospheric clouds

Mesospheric CO₂ ice clouds have been observed at different times of day, and González-Galindo et al. (2011) already showed through MGCM simulations that the formation altitude follows the propagation of the diurnal tide in the Martian atmosphere. The observations showed also a clear seasonality and longitudinal distribution that was closely reproduced by the MGCM (González-Galindo et al., 2011). We are looking into these aspects with Figures 15, 16 and 17.

Figure 15 reveals the behavior of the CO₂ ice column density as a function of local time and solar longitude in the equatorial mesosphere (above 10 Pa and between $\pm 15^\circ$ N) in the simulation MPCO2+H2OCN and compares the result with CO₂ ice cloud observations from the same latitude range. The clouds form in the model essentially during nighttime and morning, up to early afternoon during the first half of the Martian Year. Maximum column densities are found between 9 AM and 1 PM around $L_s=30^\circ$ and again, after the aphelion pause, around $L_s=100^\circ$. The decrease in ice formation during the afternoon hours in the model is striking in comparison with the observations that cluster between LT 14-18. In the afternoon almost no ice is produced by the model, and the rare morning observations are found during a season in which the model displays a clear pause in cloud formation.

In what follows, we investigate the possible causes of these disagreements with observational data. We have plotted longitude- L_s Hovmöller diagrams (Hovmöller, 1949) of CO₂ ice mixing ratio and temperature (Fig. 16). Cloud formation (shown as mixing ratios in the top panel of Fig. 16) and the temperature minima (bottom panel of Fig. 16) are strongly correlated, as expected. There is an evident pause in cloud formation (top panel of Fig. 16) between $L_s=40^\circ$ and $L_s=80^\circ$ and again during the latter half of the year from $L_s=220^\circ$ until about $L_s=320^\circ$. The second pause is related to globally higher temperatures (150-170 K) at the mesospheric CO₂ ice cloud formation altitude during the southern summer (bottom panel of Fig. 16), caused by the dustier atmosphere during this season. Concerning the

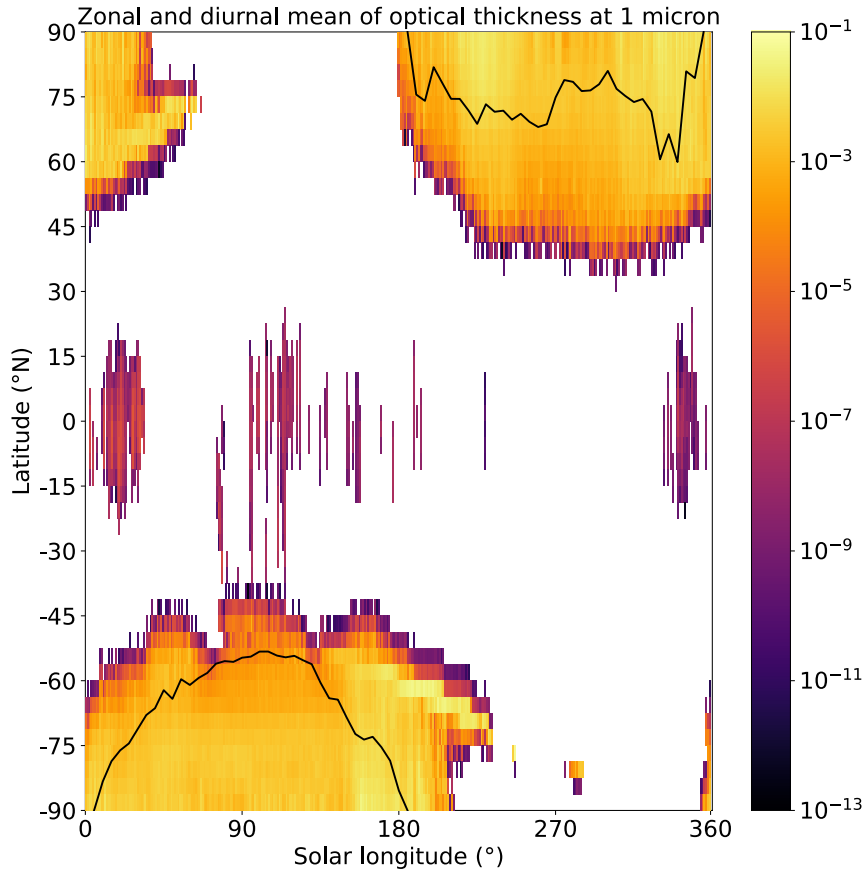


Figure 14: Zonal and diurnal mean of the CO₂ ice optical thickness at 1 μm for MPCO₂+H₂OCN simulation. The solid black line shows the limits of the supersaturated area in the polar nights (Hu et al., 2012).

605 aphelion season, Fig. 16 (bottom panel) reveals that at these altitudes the highest temperatures (about 180 K) are actually
 606 modeled during this season, and they display a wave 3 structure as a function of longitude. Generally, temperatures
 607 are too high at these altitudes during $L_s=40-80^\circ$ for clouds to form in the model. The increase of temperature in the
 608 $L_s=40-80$ interval is not produced by changes in the radiative heating terms, instead it seems related to a change in
 609 the dynamical structure predicted by the model (not shown). Zonal winds, which before $L_s=40$ are westward at the
 610 equator, become eastward, and go back to westward after $L_s=80$. Unfortunately measurements of mesospheric winds
 611 are very scarce. Nevertheless, as the observations also show a lull in cloud formation, although at later in the season
 612 ($L_s=60-100^\circ$, see Fig. 13), the predicted increase of mesospheric temperatures is probably not false, although it may
 613 be stronger and/or shifted in time with respect to reality.

614 We are also showing longitude–local time Hovmöller diagrams of CO₂ ice mixing ratio and temperature averaged
 615 over a Martian year (Fig. 17) to study two aspects: first, the cloud formation during daytime, and second, the source
 616 of the maximum of cloud formation frequency around -45°E longitude seen in Fig. 2. The top panel of Fig. 17
 617 shows that the only region where clouds form during daytime (12–15 LT) is a longitudinal corridor between 0 and
 618 -50°E . This overlaps with the favored longitude range of cloud formation revealed by the observations (Määttänen
 619 and Montmessin, 2021), but the modeled longitude range is narrower than the observed one. The cloud formation
 620 maximum within this longitude range was already seen in the cloud occurrence frequency (Fig. 2) where this range
 621 displayed the most frequent cloud formation at the equator throughout the Martian year. The bottom panel of Fig. 17
 622 shows the temperature structure related to the cloud formation, and as expected, cloud formation is directly correlated
 623 with modeled temperature minima. The non-migrating tides that are related to the surface topography are here the main
 624 drivers of the wave structures (González-Galindo et al., 2011) that are seen propagating over longitudes as a function
 625 of local time at these altitudes (at pressures less than 10 Pa). The coldest temperatures are related to a wave propagating

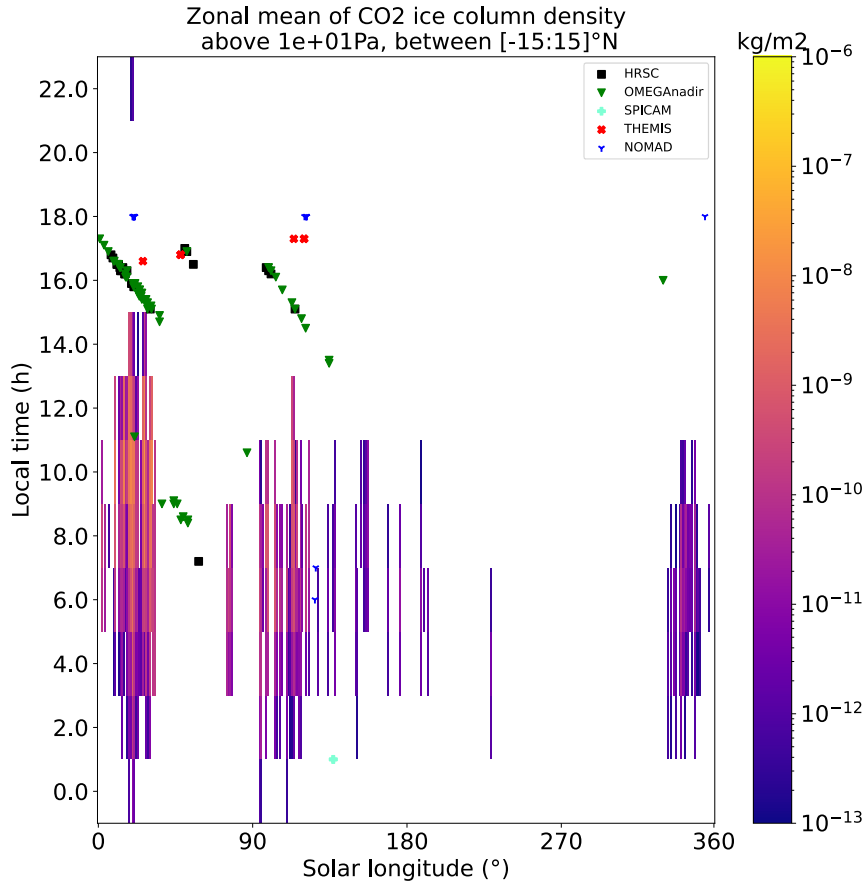


Figure 15: Local time evolution of the zonal mean CO₂ column density between $\pm 15^\circ\text{N}$ and above 10 Pa as a function of solar longitude, for MPCO2+H2OCN simulation. In the same latitude range, observational data comes from: black square = HRSC, green triangle = OMEGA, red X = THEMIS, cyan + = SPICAM, and blue "Y" = NOMAD.

626 between -100°E and 50°E over the course of the day, with the maximum CO₂ ice mixing ratios modeled during and
 627 propagating with its coldest phase, between midnight and 15 LT. Fig. 17 reinforces the evidence on migrating and
 628 non-migrating tides being the main drivers of the regions where CO₂ ice clouds form in the Martian mesosphere
 629 (González-Galindo et al., 2011). However, our MGCM is not yet reproducing all of the the subtleties of the observed
 630 cloud distribution. This must be due to processes not yet taken into account or only partially reproduced in the MGCM
 631 (CN sources, CO₂ ice cloud radiative effects, etc.). The effects of small-scale non-orographic gravity waves are not
 632 included in these simulations, and they are known to modify the mesospheric thermal structure and the tides (Gilli
 633 et al., 2020).

634 Figures 16 and 17 show that the modeled mass mixing ratios at altitudes above 10 Pa remain below 10^{-7} . Recent
 635 observations of CO₂ ice clouds by the NOMAD instrument in solar occultation (Liuzzi et al., 2021) revealed mass
 636 mixing ratios between 10^{-5} and $5 \cdot 10^{-4}$, two orders of magnitude or more higher than the values obtained by our
 637 model.

638 3.3.3. Mesospheric cloud particle radii

639 Some observations have allowed for extracting information on particle sizes in the mesospheric CO₂ ice clouds
 640 (see, e.g., Montmessin et al., 2006, 2007; Määttänen et al., 2010; Clancy et al., 2019; Liuzzi et al., 2021). The first
 641 datasets pointed to large, up to $r_{\text{eff}} \approx 1 \mu\text{m}$ effective radii near the equator during the day (Montmessin et al., 2007;
 642 Määttänen et al., 2010), and smaller, submicrometer-sized ($r_{\text{eff}} \approx 100 \text{ nm}$) particles during the night in tropical and
 643 midlatitudes (Montmessin et al., 2006). More recent work (Clancy et al., 2019; Liuzzi et al., 2021) reported an increase
 644 in particle size during the night, however at much lower altitudes (45-60 km) than the submicron crystals observed at

Global CO₂ microphysics for Mars

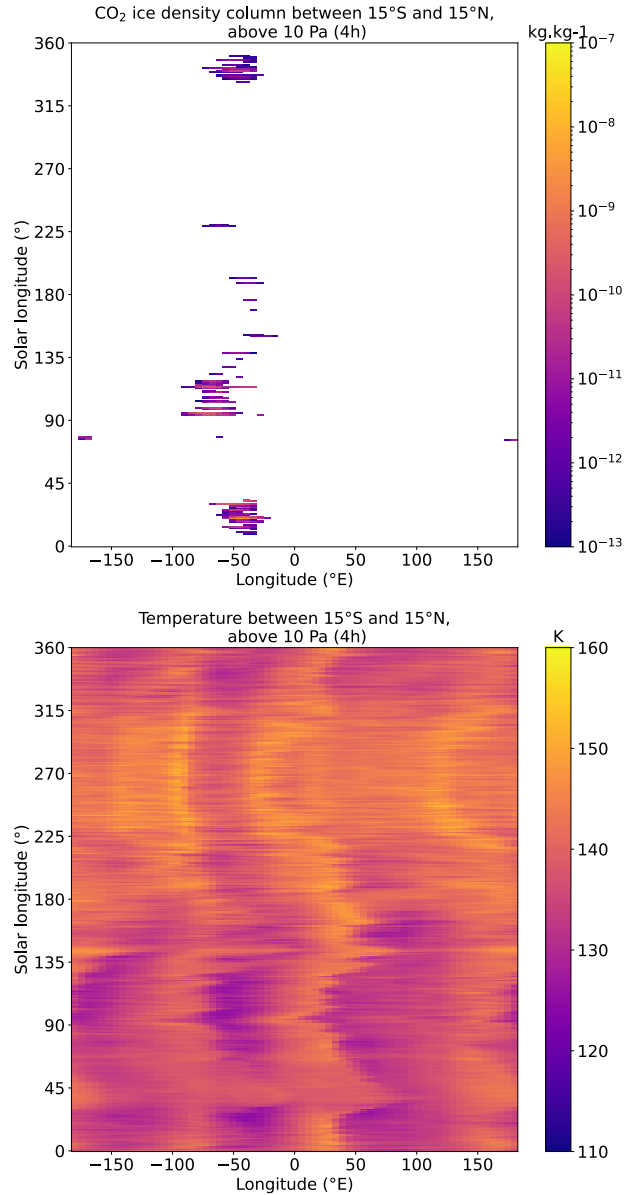


Figure 16: Longitude- L_s Hovmöller diagrams (Hovmöller, 1949) of CO₂ ice mixing ratio (top) and temperature (bottom) between 15°N and 15°S at altitudes above the 10 Pa pressure level at 4 AM.

645 100 km by Montmessin et al. (2006). In previous work, Colaprete et al. (2008) modeled equatorial mesospheric clouds
 646 with mean radii between 1 and 10 μm .

647 Figure 18 shows the zonal and annual mean of the crystal radii at the equator as a function of local time (LT). On
 648 average, the radii do not vary in the model as much as in the observations, staying in the submicron range at all local
 649 times, and their 1- σ variability is not large. Submicron-size particles were also observed during the night by SPICAM
 650 in stellar occultation, although the observations were not made at the equator but around 15°S and 35°S: Montmessin
 651 et al. (2006) reported particles of ≈ 100 nm at high altitudes (100 km) around midnight. It should be kept in mind that
 652 there no afternoon clouds (15-20 LT) are predicted by the model.

653 Clancy et al. (2019) reported observations of lower altitude (60 km) CO₂ ice clouds during the night (3 LT), best
 654 fitted with far larger particle sizes (7 μm effective radius) than during the day. Also Liuzzi et al. (2021) reported larger
 655 crystals at dawn than at dusk. There is no indication of a large-particle nighttime cloud population in our model results,

Global CO₂ microphysics for Mars

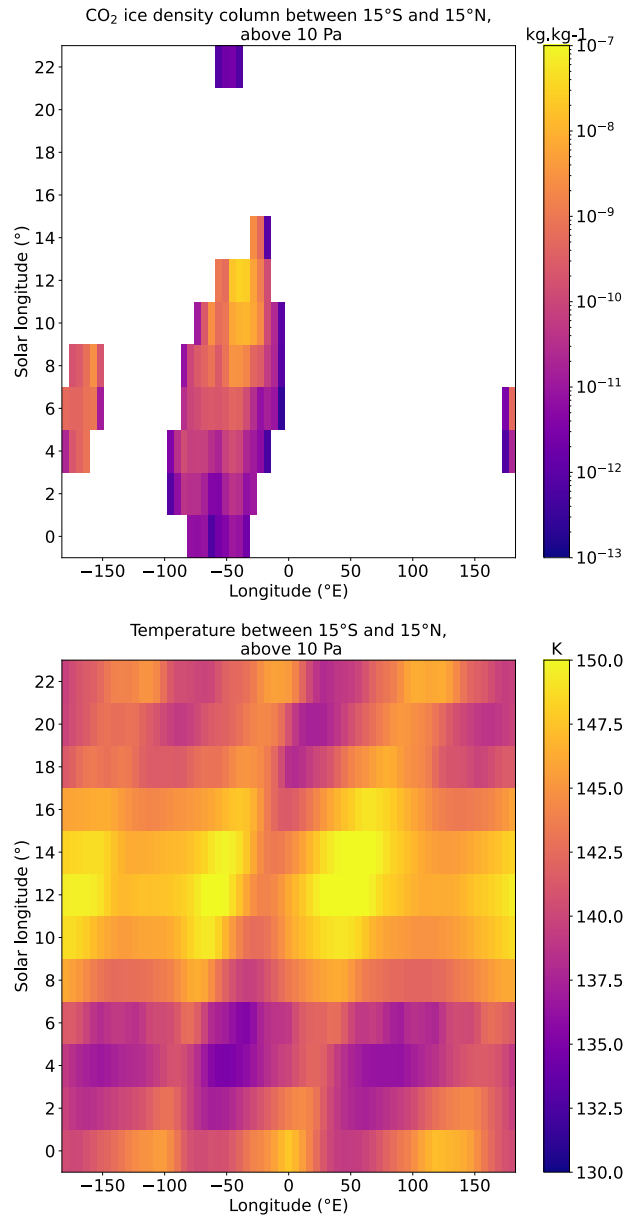


Figure 17: Longitude–Local time Hovmöller diagrams of the annual mean of CO₂ ice mixing ratio (top) and temperature (bottom) between 15°N and 15°S at altitudes above the 10 Pa pressure level.

656 but Figure 18 does show a small trend of increasing particle sizes during the night, although the particle sizes are around
 657 100 nm even at their maximum.

658 The cloud altitudes are the highest at midnight (approximately 70 km) and the altitude decreases steadily throughout
 659 the night and the morning (down to 40 km).

660 A detailed comparison with the observations will be performed when future simulations accounting for all CN
 661 sources in the mesosphere are available.

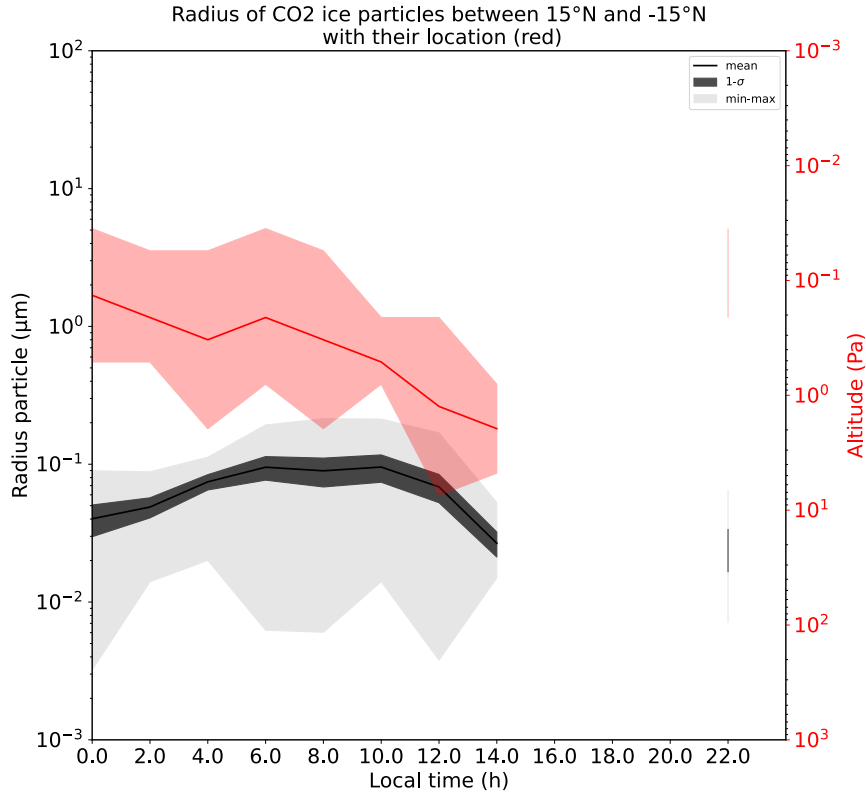


Figure 18: Zonal and annual mean of the crystal radii between 15°N and 15°S as a function of local time (black line), its 1- σ variability (dark grey shading) and the full variability (light grey shading). Also shown is the mean altitude (in Pa, red line) of the clouds with the full variability range (red shading).

662 4. Summary and conclusions

663 This paper presents the first 3D global CO₂ ice cloud modeling results accounting for a condensation theory
664 adapted for the highly supersaturated near-pure vapor conditions of the Martian atmosphere and water ice crystals
665 as condensation nuclei.

666 The coupling of the previously developed microphysical CO₂ ice cloud model with the 3D MGCM has been
667 successfully completed and the first simulations have been analyzed. The MGCM produces CO₂ ice clouds both in the
668 polar night troposphere and in the summer mesosphere at low latitudes. We show that the latter are only forming when
669 the model uses water ice crystals as condensation nuclei: mineral dust lofted from the surface to the mesosphere is not
670 sufficient as CN. Despite the good agreement of the modeled spatial and seasonal cloud distributions, the modeled CO₂
671 ice cloud optical depths are several orders of magnitude below those observed, confirming the need of an additional
672 CN source in the mesosphere, which could be provided by particles formed after meteor ablation. Mesospheric CO₂ ice
673 cloud crystal radii are in the submicron range and do not reach the maximum values observed (around 1 μm). Daytime
674 mesospheric CO₂ ice clouds are lacking in the model, and this is directly related to the modeled temperature structure
675 that is generally too warm around the equator in the afternoon. The reasons for this need to be investigated further, but
676 might be explained by lacking subgrid scale processes such as the effect of gravity waves on the temperatures.

677 The polar clouds extend to higher altitudes than observed and the cloud formation season is longer than the observed
678 one: overall, the modeled polar atmosphere is colder than what the observations show, revealed by the very deep
679 supersaturated polar atmosphere in the model. This might be due to the too high prescribed dust column optical depth
680 in the polar regions, poorly constrained by lacking observations in the polar regions. Polar cloud crystal sizes go up to
681 some tens of microns, in the lower range of the observed estimates. Snowfall from polar clouds contributes up to 10%
682 of the ice flux to the polar cap ice, which is within the surface ice contribution estimated from observations. This CO₂

683 snowfall also slightly modifies the longitudinal and seasonal variation of the surface ice mass compared to the case
684 without detailed CO₂ ice cloud microphysics.

685 The formation of CO₂ ice clouds on water ice crystals and the subsequent scavenging of the ice leads to a
686 modification of the water ice and vapor distribution in the Martian atmosphere and can also impact radiative fluxes.
687 These aspects are not studied in the current paper, but the new CO₂ ice cloud microphysics provide us with the means
688 of investigating the coupling between the water and CO₂ cycles through clouds and the role of this coupling in the
689 Martian climate system.

690 Here we have presented the reference configuration of the cloud simulations, but further developments are on the
691 way. They include using an additional CN source in the mesosphere (nanoparticles of meteoric origin) and accounting
692 for the radiative effect of the CO₂ ice clouds. The results of these developments will be reported in dedicated,
693 forthcoming papers.

694 Acknowledgments

695 This paper presents the results of ten years of development that has been supported by funding from several sources.
696 We thank the Agence National de la Recherche for funding (projet MECCOM, ANR-18-CE31-0013). We are also
697 grateful for the financial support by the LabEx (Laboratoire d'Excellence) ESEP, by the French space agency CNES and
698 the European Space Agency ESA. We acknowledge the support of the French national planetology programme (PNP)
699 as well. This work was performed using HPC computing resources from GENCI-CINES (Grant 2021-A0100110391),
700 and resources at the ESPRI mesocentre of the IPSL institute.

701 Data availability

702 The simulation outputs will be archived by the acceptance of the paper at the ESPRI mesocentre where the archive
703 will also receive a DOI. We are currently in the process of preparing the final files for the archive.

704 A. Appendix: Model validation and convergence

705 We have performed simulations of three consecutive Martian years to reach a convergence of the simulated year-
706 to-year climate. This is particularly important for the water cycle, as it takes a long time for it to converge. In some
707 of our simulations the new CO₂ ice cloud microphysics is coupled with the water cycle, which might perturb the
708 water cycle and lead to less rapid convergence. We have checked convergence by interannual stability of the amount of
709 water ice and the repeatability of the water cycle and the temperature variations. We also compare TES observations
710 of water vapor and ice (Smith, 2002) with our simulated water vapor and ice from MGCM outputs (see Figs. 19 and
711 20). This comparison of our reference simulation (right panel in Figs. 19 and 20) and a reference run with full water
712 ice microphysics but no CO₂ ice microphysics (middle panel of Figs. 19 and 20) to TES observations (left panel in
713 Figs. 19 and 20) shows that the modeled water cycle is very similar in both simulations and that the differences to the
714 observations are similar as well, as already reported in Navarro et al. (2014). The similarity of the water cycles in the
715 two simulations shows that the inclusion of the new CO₂ ice microphysics does not profoundly perturb the water cycle
716 that remains consistent between the simulations and the observations.

717 Figures 21, 22 and 23 represent global means of primary variables at the surface: pressure, temperature, and total
718 surface CO₂ ice mass. Each simulated year is represented by its number and color, from deep blue (year 1) through
719 green (year 2) to dark red (year 3). Surface pressure, surface temperature and surface CO₂ ice overlap well, expect
720 for small interannual variations. For surface pressure and surface CO₂ ice, that are linked, these variations are seen in
721 some years between sols 0 and 180 and again from sol 600 until the end of the year. The average surface temperature
722 shows more generalized interannual variations that are related to the natural variability of the system. Despite reaching
723 an overall convergence, the total atmospheric water in the simulations shows interannual variations depending on the
724 model configuration. We have chosen to take the results from the third year of simulations to compare with the others.
725 We show for all simulations the amount of total mass of atmospheric water in Fig. 24. Despite the differing absolute
726 values, the similar overall behavior of the water cycles ensures that our simulation comparison is consistent. The large
727 difference and trends in total water seen between the simulations (lowest panel in Fig. 24) is within the known variability
728 of the water cycle behavior in the model.

Global CO₂ microphysics for Mars

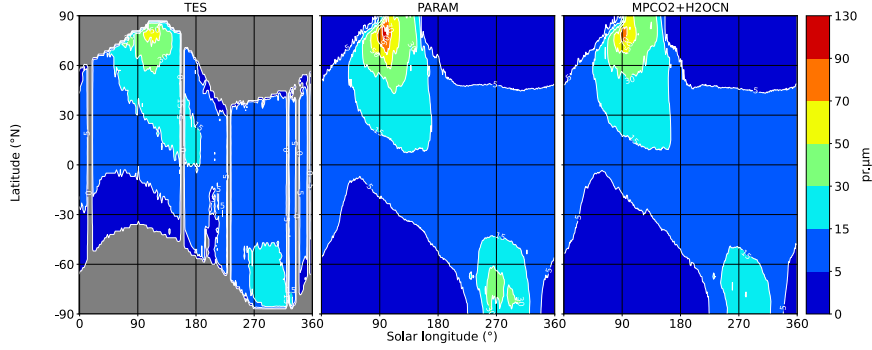


Figure 19: Annual variation of the zonal mean water vapor column (in precipitable micrometers) from (left) TES observations, (middle) a reference simulation without CO₂ microphysics, and (right) the MPCO₂+H₂OCN simulation.

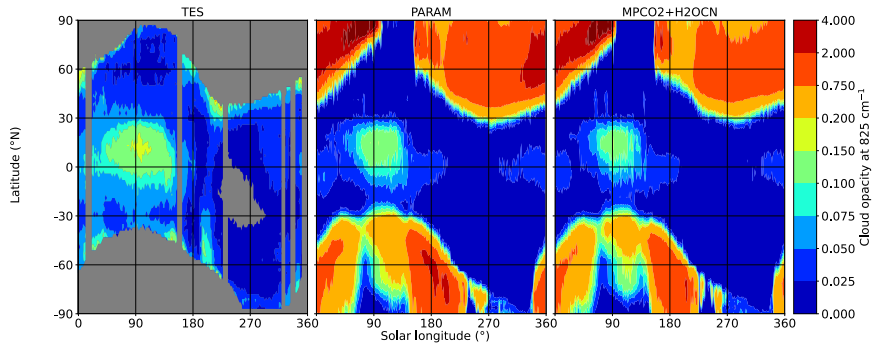


Figure 20: Annual variation of the zonal mean water ice optical depth from (left) TES observations, (middle) a reference simulation without CO₂ microphysics, and (right) the MPCO₂+H₂OCN simulation.

729 **B. Appendix: The analytical expression for growth rate of Martian CO₂ crystals**

730 We present here a new analytical expression for the growth rate of Martian CO₂ crystals, applicable to a near-pure,
731 highly supersaturated gas.

732 **B.1. New equation for the crystal surface temperature T_a**

The equation (6) of Listowski et al. (2014) (here Eq. 3) gives the solution for the system of three, coupled equations (mass transfer rate, particle surface temperature, partial vapor pressure at the crystal surface) that govern the growth of a particle. Eq. 3 iteratively solves the system of equations for the crystal surface temperature T_a that is needed for finding the growth rate of the crystal. To this end, we need to find the solution $f_C(T_a) = 0$ for:

$$f_C(T_a) = T_a + c_0 \exp(c_1 T_a) - c_2, \quad (3)$$

where

$$\begin{aligned} c_0 &= \frac{M_v D p_{sat} L_{sub}}{RT_\infty K} S_{eq} \exp\left(\frac{-L_{sub} M_v}{RT_\infty}\right), \\ c_1 &= \frac{L_{sub} M_v}{RT_\infty^2}, \\ c_2 &= T_\infty + \frac{M_v D L_{sub}}{K R T_\infty} p_{v,\infty}. \end{aligned} \quad (4)$$

733 In these equations the following parameters are used: M_v the molar mass of the condensing vapor (CO₂, 44.03 g
734 mol⁻¹), D the binary diffusion coefficient of CO₂ in N₂, p_{sat} the saturation vapor pressure of CO₂ (James et al.,

Global CO₂ microphysics for Mars

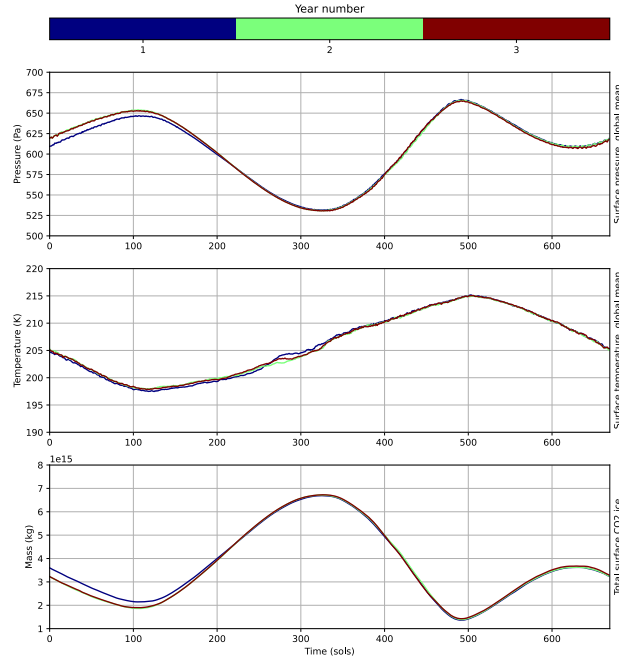


Figure 21: PARAM simulation, convergence of global mean values as a function of sol for surface pressure, surface temperature, and surface CO₂ ice mass.

735 1992), L_{sub} the latent heat of sublimation (Listowski et al., 2013), R the gas constant, T_{∞} is the temperature of the
 736 environment (far from the surface of the particle), K the thermal conductivity of the gas mixture CO₂/N₂, and $p_{v,\infty}$ the
 737 partial vapor pressure at the particle surface. S_{eq} is the Kelvin factor that accounts for the effect of the surface curvature:
 738 $S_{eq} = \exp(2\sigma M_v / a\rho_{ice} RT_{\infty})$, where σ is the surface energy of CO₂ ice (0.08 J m⁻²), ρ_{ice} is the density (1600 kg m⁻³)
 739 of CO₂ ice (Wood, 1999) and a is the particle radius. The coefficients D and K are defined as in Listowski et al. (2013)
 740 and take into account the Fuchs and Sutugin (1970) correction for the flow regime.

It can be shown that if we insert the values of the different parameters in c_2 , and by using the mole fraction x_v we can write $p_{v,\infty} = x_v \times p$ when $x_v \rightarrow 1$ (near-pure vapor), we get:

$$\left(\frac{M_v DL_{sub}}{K RT_{\infty}} p_{v,\infty} \right) \gg T_{\infty}. \quad (5)$$

741 Please note that this inequality is not valid for $x_v \rightarrow 0$ (a trace gas).

Thus we get:

$$c_2 \simeq \frac{M_v DL_{sub}}{K RT_{\infty}} p_{v,\infty} \quad (6)$$

Thus, since T_a et T_{∞} are of the same order of magnitude, we can suppose that $\left(\frac{M_v DL_{sub}}{K RT_{\infty}} p_{v,\infty} \right) \gg T_a$ and the equation (3) becomes:

$$f_C(T_a) \simeq c_0 \exp(c_1 T_a) - c_2. \quad (7)$$

Now solving $f_C(T_a)$ iteratively is not anymore necessary and we get

$$T_a = \frac{1}{c_1} \ln \left(\frac{c_2}{c_0} \right). \quad (8)$$

Global CO₂ microphysics for Mars

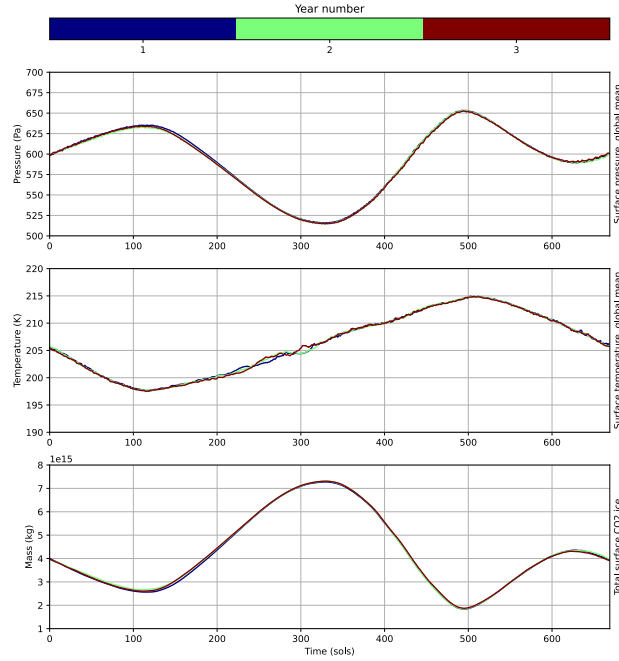


Figure 22: Same as 21, but for MPCO2 simulation.

According to the coefficients given in equations (4) and using the approximation for c_2 (equation 6), we can write:

$$\frac{c_2}{c_0} \sim \frac{p_{v,\infty}}{p_{sat} \times S_{eq}} \exp\left(\frac{L_{sub} M_v}{RT_\infty}\right). \quad (9)$$

Then with the definition $S = \frac{p_{v,\infty}}{p_{sat}}$, combining (8) and (9), we get:

$$T_a = T_\infty + \frac{1}{c_1} \ln\left(\frac{S}{S_{eq}}\right), \quad (10)$$

742 where c_1 is as defined in equations (4).

743 B.2. New growth rate dr/dt and the associated error

For calculating the growth rate we write (see Listowski et al., 2014, equation (8)):

$$\frac{dr}{dt} = -\frac{1}{4\pi r^2 \rho_{ice}} I_m = -\frac{1}{4\pi r^2 \rho_{ice}} \frac{4\pi r K}{L_{sub}} (T_\infty - T_a). \quad (11)$$

Inserting Eq. (10) we get:

$$\frac{dr}{dt} = \frac{K R T^2}{r \rho_{ice} L_{sub}^2 M_v} \ln\left(\frac{S}{S_{eq}}\right). \quad (12)$$

744 By comparing the growth rates determined with T_a calculated using Eq. (3), the exact solution, and Eq. (10), the
 745 new approximative solution, we obtain a relative error of $\leq 0.6\%$ for a large range of conditions that are valid for the
 746 present-day Mars (pressure ~ 100 Pa-0.0001 hPa, saturation ratio ~ 1.001 -1000, and CO₂ mole fraction ~ 0.75 - 0.96).

747 B.3. Link with the linearized growth rate expression

In the case of the linearized expression, valid for a trace gas and/or small saturation ratios we get:

$$T_a = T_\infty + \frac{\rho_{ice} L_{sub}}{K(R_d + R_h S_{eq})} (S - S_{eq}). \quad (13)$$

Global CO₂ microphysics for Mars

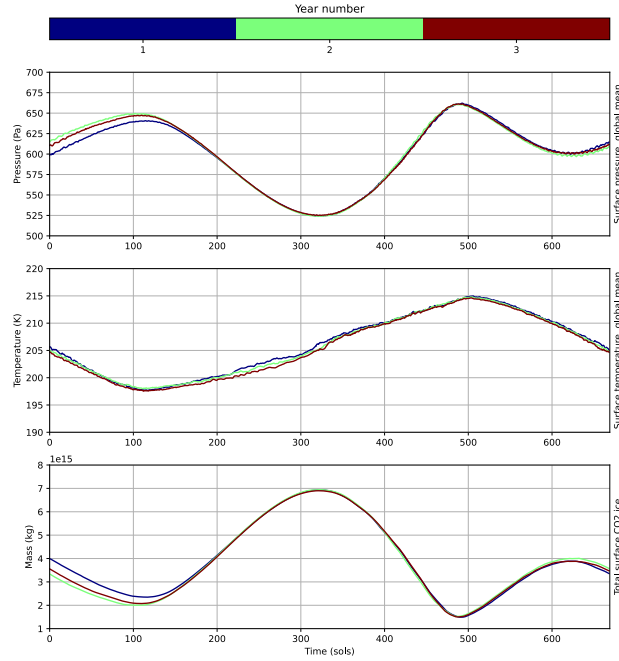


Figure 23: Same as 21, but for MPCO2+H2OCN simulation.

748 If $S \rightarrow S_{\text{eq}}$, $\ln\left(\frac{S}{S_{\text{eq}}}\right) \sim \left(\frac{S}{S_{\text{eq}}} - 1\right)$, Eq. (10) becomes equivalent to the linearized equation (Eq. (13)). This requires
 749 also to note that $\frac{\rho_{\text{ice}} L_{\text{sub}}}{K(R_d + R_h S_{\text{eq}})} (S - S_{\text{eq}}) \sim \frac{1}{c_1 S_{\text{eq}}}$ requiring a scale analysis of the different terms.

750 References

- 751 Aoki, S., Sato, Y., Giuranna, M., Wolkenberg, P., Sato, T., Nakagawa, H., Kasaba, Y., 2018. Mesospheric CO₂ ice clouds on Mars observed by
 752 Planetary Fourier Spectrometer onboard Mars Express. *Icarus* 302, 175–190. URL: <http://www.sciencedirect.com/science/article/pii/S0019103516306340>, doi: <https://doi.org/10.1016/j.icarus.2017.10.047>.
- 754 Benson, J.L., Kass, D.M., Kleinböhl, A., 2011. Mars' north polar hood as observed by the Mars Climate Sounder. *Journal of Geophysical Research (Planets)* 116, 3008. doi:10.1029/2010JE003693.
- 756 Benson, J.L., Kass, D.M., Kleinböhl, A., McCleese, D.J., Schofield, J.T., Taylor, F.W., 2010. Mars' south polar hood as observed by the Mars
 757 Climate Sounder. *J. Geophys. Res.* 115, 12015. doi:10.1029/2009JE003554.
- 758 Clancy, R.T., Wolff, M.J., Smith, M.D., Kleinböhl, A., Cantor, B.A., Murchie, S.L., Toigo, A.D., Seelos, K., Lefèvre, F., Montmessin, F., Daerden, F.,
 759 Sandor, B.J., 2019. The distribution, composition, and particle properties of mars mesospheric aerosols: An analysis of crism visible/near-ir limb
 760 spectra with context from near-coincident mcs and marci observations. *Icarus* 328, 246–273. doi: <https://doi.org/10.1016/j.icarus.2019.03.025>.
- 762 Clancy, R.T., Wolff, M.J., Whitney, B.A., Cantor, B.A., Smith, M.D., 2007. Mars equatorial mesospheric clouds: Global occurrence and physical
 763 properties from Mars Global Surveyor Thermal Emission Spectrometer and Mars Orbiter Camera limb observations. *J. Geophys. Res.* 112,
 764 E04004. doi:10.1029/2006JE002805.
- 765 Colaprete, A., Barnes, J.R., Haberle, R.M., Montmessin, F., 2008. CO₂ clouds, CAPE and convection on Mars: observations and general circulation
 766 modeling. *Planet. Space Sci.* 56, 150–180. doi:10.1016/j.pss.2007.08.010.
- 767 Colaprete, A., Haberle, R.M., Toon, O.B., 2003. Formation of convective carbon dioxide clouds near the south pole of Mars. *Journal of Geophysical
 768 Research* 108.
- 769 Colaprete, A., Toon, O.B., 2002. Carbon dioxide snow storms during the polar night on Mars. *Journal of Geophysical Research* 107.
- 770 Crismani, M.M.J., Schneider, N.M., Plane, J.M.C., Evans, J.S., Jain, S.K., Chaffin, M.S., Carrillo-Sanchez, J.D., Deighan, J.I., Yelle, R.V., Stewart,
 771 A.I.F., McClintock, W., Clarke, J., Holsclaw, G.M., Stiepen, A., Montmessin, F., Jakosky, B.M., 2017. Detection of a persistent meteoric metal
 772 layer in the Martian atmosphere. *Nature Geoscience* 10, 401–404. doi:10.1038/ngeo2958.
- 773 Duft, D., Nachbar, M., Leisner, T., 2019. Unravelling the microphysics of polar mesospheric cloud formation. *Atmospheric Chemistry and Physics*
 774 19, 2871–2879. URL: <https://acp.copernicus.org/articles/19/2871/2019/>, doi:10.5194/acp-19-2871-2019.

Global CO₂ microphysics for Mars

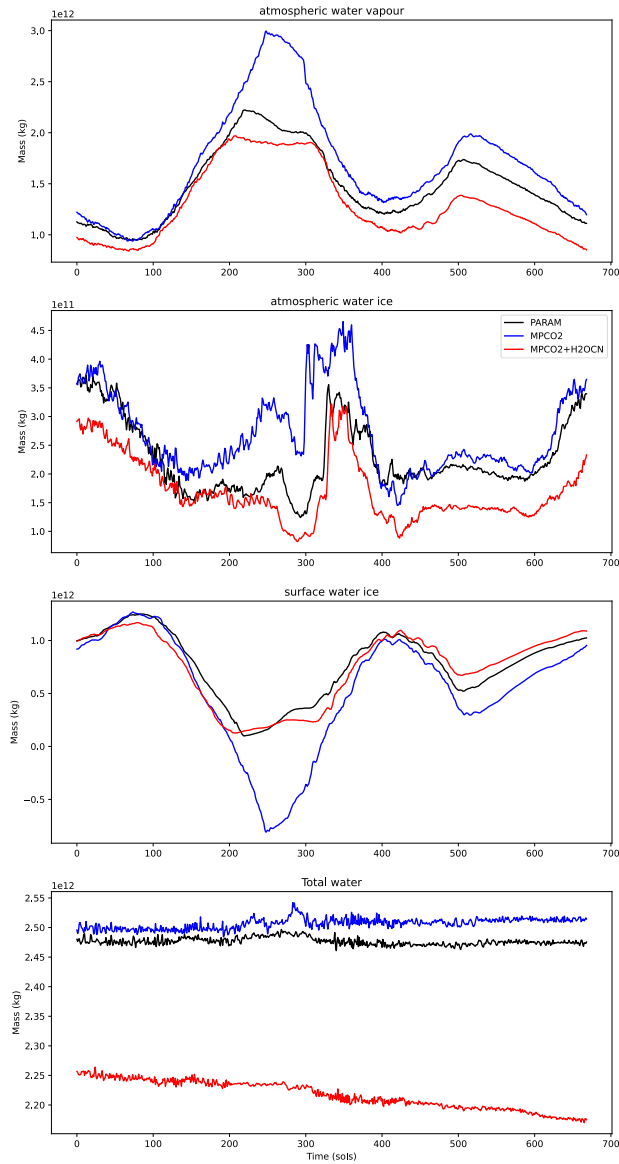


Figure 24: Water reservoirs in Mars during a year from top to bottom: atmospheric water vapour, atmospheric water ice, surface water ice, and total water mass. Colors indicate the simulation: PARAM in black, MPCO2 in blue, and MPCO2+H2OCN in red.

- 775 Fedorova, A., Montmessin, F., Rodin, A., Korabiev, O., Määttänen, A., Maltagliati, L., Bertaux, J.L., 2014. Evidence for a bimodal size distribution
 776 for the suspended aerosol particles on mars. *Icarus* 231, 239–260. URL: [https://www.sciencedirect.com/science/article/pii/](https://www.sciencedirect.com/science/article/pii/S0019103513005332)
 777 [S0019103513005332](https://doi.org/10.1016/j.icarus.2013.12.015), doi:<https://doi.org/10.1016/j.icarus.2013.12.015>.
- 778 Forget, F., Hansen, G.B., Pollack, J.B., 1995. Low brightness temperatures of Martian polar caps: CO₂ clouds or low surface emissivity? *J. Geophys.*
 779 *Res.* 100, 21219–21234. doi:10.1029/95JE02378.
- 780 Forget, F., Hourdin, F., Fournier, R., Hourdin, C., Talagrand, O., Collins, M., Lewis, S.R., Read, P.L., Huot, J.P., 1999. Improved general circulation
 781 models of the martian atmosphere from the surface to above 80 km. *J. Geophys. Res.* 104, 24155–24176. doi:10.1029/1999JE001025.
- 782 Forget, F., Hourdin, F., Talagrand, O., 1998. CO₂ snowfall on Mars: Simulation with a general circulation model. *Icarus* 131, 302–316.
 783 doi:10.1006/icar.1997.5874.
- 784 Forget, F., Montmessin, F., Bertaux, J.L., González-Galindo, F., Lebonnois, S., Quémerais, E., Reberac, A., Dimarellis, E., López-Valverde, M.A.,
 785 2009. The density and temperatures of the upper martian atmosphere measured by stellar occultations with Mars Express SPICAM. *J. Geophys.*
 786 *Res.* 114, E01004. Doi:10.1029/2008JE003086.
- 787 Fuchs, N.A., Sutugin, A.G., 1970. Highly dispersed aerosols. *Ann Arbor Science Publ., Ann Arbor, Michigan.*

- 788 Gilli, G., Forget, F., Spiga, A., Navarro, T., Millour, E., Montabone, L., Kleinböhl, A., Kass, D.M., McCleese, D.J., Schofield, J.T.,
789 2020. Impact of gravity waves on the middle atmosphere of mars: A non-orographic gravity wave parameterization based on
790 global climate modeling and mcs observations. *Journal of Geophysical Research: Planets* 125, e2018JE005873. URL: <https://agupubs.onlinelibrary.wiley.com/doi/abs/10.1029/2018JE005873>,
791 [doi:https://doi.org/10.1029/2018JE005873](https://doi.org/10.1029/2018JE005873),
792 [arXiv:https://agupubs.onlinelibrary.wiley.com/doi/pdf/10.1029/2018JE005873](https://arxiv.org/abs/https://agupubs.onlinelibrary.wiley.com/doi/pdf/10.1029/2018JE005873). e2018JE005873 10.1029/2018JE005873.
- 793 Glandorf, D.L., Colaprete, A., Tolbert, M.A., Toon, O.B., 2002. CO₂ Snow on Mars and Early Earth: Experimental Constraints. *Icarus* 160, 66–72.
794 [doi:10.1006/icar.2002.6953](https://doi.org/10.1006/icar.2002.6953).
- 795 González-Galindo, F., Forget, F., López-Valverde, M.A., i Coll, M.A., Millour, E., 2009. A ground-to-exosphere martian general circulation model:
796 I. seasonal, diurnal and solar cycle variation of thermospheric temperatures. *J. Geophys. Res.* 114, E04001. [Doi:10.1029/2008JE003246](https://doi.org/10.1029/2008JE003246).
- 797 González-Galindo, F., Määttänen, A., Forget, F., Spiga, A., 2011. The martian mesosphere as revealed by CO₂ cloud observations and General
798 Circulation Modeling. *Icarus* 216, 10–22. [doi:10.1016/j.icarus.2011.08.006](https://doi.org/10.1016/j.icarus.2011.08.006).
- 799 Hayne, P.O., Paige, D.A., Heavens, N.G., 2014. The role of snowfall in forming the seasonal ice caps of mars: Models and constraints from the
800 mars climate sounder. *Icarus* 231, 122 – 130. URL: <http://www.sciencedirect.com/science/article/pii/S0019103513004491>,
801 [doi:https://doi.org/10.1016/j.icarus.2013.10.020](https://doi.org/10.1016/j.icarus.2013.10.020).
- 802 Hayne, P.O., Paige, D.A., Schofield, J.T., Kass, D.M., Kleinböhl, A., Heavens, N.G., McCleese, D.J., 2012. Carbon dioxide snow clouds on mars:
803 South polar winter observations by the mars climate sounder. *J. Geophys. Res. Planets* 117, n/a–n/a. URL: <http://dx.doi.org/10.1029/2011JE004040>,
804 [doi:10.1029/2011JE004040](https://doi.org/10.1029/2011JE004040). e08014.
- 805 Hovmöller, E., 1949. The trough-and-ridge diagram. *Tellus* 1, 62–66. URL: <https://onlinelibrary.wiley.com/doi/abs/10.1111/j.2153-3490.1949.tb01260.x>,
806 [doi:https://doi.org/10.1111/j.2153-3490.1949.tb01260.x](https://doi.org/10.1111/j.2153-3490.1949.tb01260.x),
807 [arXiv:https://onlinelibrary.wiley.com/doi/pdf/10.1111/j.2153-3490.1949.tb01260.x](https://onlinelibrary.wiley.com/doi/pdf/10.1111/j.2153-3490.1949.tb01260.x).
- 808 Hu, R., Cahoy, K., Zuber, M.T., 2012. Mars atmospheric CO₂ condensation above the north and south poles as revealed by radio occultation, climate
809 sounder, and laser ranging observations. *J. Geophys. Res. Planets* 117. [doi:10.1029/2012JE004087](https://doi.org/10.1029/2012JE004087).
- 810 Ivanov, A.B., Muhleman, D.O., 2001. Cloud Reflection Observations: Results from the Mars Orbiter Laser Altimeter. *Icarus* 154, 190–206.
811 [doi:10.1006/icar.2001.6686](https://doi.org/10.1006/icar.2001.6686).
- 812 Jacobson, M.Z., 2005. *Fundamentals of Atmospheric Modeling*. 2 ed., Cambridge University Press. [doi:10.1017/CB09781139165389](https://doi.org/10.1017/CB09781139165389).
- 813 James, P.B., Kieffer, H.H., Paige, D.A., 1992. The seasonal cycle of carbon dioxide on Mars, in: Kieffer, H.H., Jakosky, B.M., Snyder, C.W.,
814 Matthews, M.S. (Eds.), *Mars*. University of Arizona Press, pp. 934–968.
- 815 Jiang, F.Y., Yelle, R.V., Jain, S.K., Cui, J., Montmessin, F., Schneider, N.M., Deighan, J., Gröller, H., Verdier, L., 2019. Detection
816 of mesospheric co₂ ice clouds on mars in southern summer. *Geophysical Research Letters* 46, 7962–7971. URL: <https://agupubs.onlinelibrary.wiley.com/doi/abs/10.1029/2019GL082029>,
817 [doi:https://doi.org/10.1029/2019GL082029](https://doi.org/10.1029/2019GL082029),
818 [arXiv:https://agupubs.onlinelibrary.wiley.com/doi/pdf/10.1029/2019GL082029](https://arxiv.org/abs/https://agupubs.onlinelibrary.wiley.com/doi/pdf/10.1029/2019GL082029).
- 819 Knollenberg, R.G., Hunten, D.M., 1980. The microphysics of the clouds of Venus - Results of the Pioneer Venus particle size spectrometer
820 experiment. *J. Geophys. Res.* 85, 8039–8058. [doi:10.1029/JA085iA13p08039](https://doi.org/10.1029/JA085iA13p08039).
- 821 Kuroda, T., Medvedev, A.S., Kasaba, Y., Hartogh, P., 2013. Carbon dioxide ice clouds, snowfalls, and baroclinic waves in the northern winter polar
822 atmosphere of mars. *Geophys. Res. Lett.* 40, 1484–1488. URL: <http://dx.doi.org/10.1002/grl.50326>, [doi:10.1002/grl.50326](https://doi.org/10.1002/grl.50326).
- 823 Lefèvre, F., Bertaux, J.L., Clancy, R.T., Encrenaz, T., Fast, K., Forget, F., Lebonnois, S., Montmessin, F., Perrier, S., 2008. Heterogeneous chemistry
824 in the atmosphere of Mars. *Nature* 454, 971–975. [doi:10.1038/nature07116](https://doi.org/10.1038/nature07116).
- 825 Lefèvre, F., Lebonnois, S., Montmessin, F., Forget, F., 2004. Three-dimensional modeling of ozone on mars. *J. Geophys. Res.* 109, E07004.
826 [Doi:10.1029/2004JE002268](https://doi.org/10.1029/2004JE002268).
- 827 Listowski, C., Määttänen, A., Montmessin, F., Spiga, A., Lefèvre, F., 2014. Modeling the microphysics of CO₂ ice clouds within wave-induced
828 cold pockets in the Martian mesosphere. *Icarus* 237, 239 – 261. URL: <http://www.sciencedirect.com/science/article/pii/S0019103514002140>,
829 [doi:https://doi.org/10.1016/j.icarus.2014.04.022](https://doi.org/10.1016/j.icarus.2014.04.022).
- 830 Listowski, C., Määttänen, A., Riipinen, I., Montmessin, F., Lefèvre, F., 2013. Near-pure vapor condensation in the Martian atmosphere: CO₂ ice
831 crystal growth. *J. Geophys. Res. Planets* 118, 2153–2171. URL: [http://dx.doi.org/10.1002/jgre.20149](https://doi.org/10.1002/jgre.20149), [doi:10.1002/jgre.20149](https://doi.org/10.1002/jgre.20149).
- 832 Liuzzi, G., Villanueva, G.L., Trompet, L., Crismani, M.M.J., Piccialli, A., Aoki, S., Lopez-Valverde, M.A., Stolzenbach, A., Daerden, F.,
833 Neary, L., Smith, M.D., Patel, M.R., Lewis, S.R., Clancy, R.T., Thomas, I.R., Ristic, B., Bellucci, G., Lopez-Moreno, J.J., Vandaele,
834 A.C., 2021. First detection and thermal characterization of terminator co₂ ice clouds with exomars/nomad. *Geophysical Research*
835 *Letters* 48, e2021GL095895. URL: <https://agupubs.onlinelibrary.wiley.com/doi/abs/10.1029/2021GL095895>, [doi:https://doi.org/10.1029/2021GL095895](https://doi.org/10.1029/2021GL095895),
836 [arXiv:https://agupubs.onlinelibrary.wiley.com/doi/pdf/10.1029/2021GL095895](https://arxiv.org/abs/https://agupubs.onlinelibrary.wiley.com/doi/pdf/10.1029/2021GL095895).
837 e2021GL095895 2021GL095895.
- 838 Määttänen, A., Douspis, M., 2014. Estimating the variability of contact parameter temperature dependence with the Monte Carlo Markov Chain
839 method. *GeoResJ* 3–4, 46 – 55. URL: <http://www.sciencedirect.com/science/article/pii/S2214242814000187>, [doi:https://doi.org/10.1016/j.grj.2014.09.002](https://doi.org/10.1016/j.grj.2014.09.002).
- 840 Määttänen, A., Montmessin, F., 2021. *Clouds in the Martian Atmosphere*. Oxford University Press. URL: <https://oxfordre.com/planetaryscience/view/10.1093/acrefore/9780190647926.001.0001/acrefore-9780190647926-e-114>,
841 [doi:10.1093/acrefore/9780190647926.013.114](https://doi.org/10.1093/acrefore/9780190647926.013.114).
- 842 Määttänen, A., Montmessin, F., Gondet, B., Scholten, F., Hoffmann, H., González-Galindo, F., Spiga, A., Forget, F., Hauber, E., Neukum, G.,
843 Bibring, J., Bertaux, J., 2010. Mapping the mesospheric CO₂ clouds on Mars: MEx/OMEGA and MEx/HRSC observations and challenges for
844 atmospheric models. *Icarus* 209, 452–469. [doi:10.1016/j.icarus.2010.05.017](https://doi.org/10.1016/j.icarus.2010.05.017).
- 845 Määttänen, A., Pérot, K., Montmessin, F., Hauchecorne, A., 2013. Mesospheric Clouds on Mars and on Earth. pp. 393–413. [doi:10.2458/azu_uapress_9780816530595-ch16](https://doi.org/10.2458/azu_uapress_9780816530595-ch16).
- 846 Määttänen, A., Vehkamäki, H., Lauri, A., Merikallio, S., Kauhanen, J., Savijärvi, H., Kulmala, M., 2005. Nucleation studies in the martian
847 atmosphere. *J. Geophys. Res.* 110, E02002. [doi:10.1029/2004JE002308](https://doi.org/10.1029/2004JE002308).

- 851 Määttänen, A., Vehkamäki, H., Lauri, A., Napari, I., Kulmala, M., 2007. Two-component heterogeneous nucleation kinetics and an application to
852 Mars. *J. Chem. Phys.* 127, 134710. doi:10.1063/1.2770737.
- 853 Madeleine, J.B., Head, J.W., Forget, F., Navarro, T., Millour, E., Spiga, A., Colaitis, A., Määttänen, A., Montmessin, F., Dickson, J.L., 2014.
854 Recent Ice Ages on Mars: The role of radiatively active clouds and cloud microphysics. *Geophys. Res. Lett.* 41, 4873–4879. doi:10.1002/
855 2014GL059861.
- 856 McConnochie, T.H., Bell, J.F., Savransky, D., Wolff, M.J., Toigo, A.D., Wang, H., Richardson, M.I., Christensen, P.R., 2010. THEMIS-
857 VIS observations of clouds in the martian mesosphere: Altitudes, wind speeds, and decameter-scale morphology. *Icarus* 210, 545–565.
858 doi:10.1016/j.icarus.2010.07.021.
- 859 Montabone, L., Forget, F., Millour, E., Wilson, R., Lewis, S., Cantor, B., Kass, D., Kleinböhl, A., Lemmon, M., Smith, M., Wolff, M., 2015.
860 Eight-year climatology of dust optical depth on mars. *Icarus* 251, 65–95. URL: [https://www.sciencedirect.com/science/article/
861 pii/S0019103515000044](https://www.sciencedirect.com/science/article/pii/S0019103515000044), doi:<https://doi.org/10.1016/j.icarus.2014.12.034>. dynamic Mars.
- 862 Montmessin, F., Bertaux, J.L., Quémerais, E., Korablev, O., Rannou, P., Forget, F., Perrier, S., Fussen, D., Lebonnois, S., Reberac, A., Dimarellis,
863 E., 2006. Subvisible CO₂ clouds detected in the mesosphere of mars. *Icarus* 183, 403–410. doi:[https://doi.org/10.1016/j.icarus.
864 2006.03.015](https://doi.org/10.1016/j.icarus.2006.03.015).
- 865 Montmessin, F., Forget, F., Rannou, P., Cabane, M., Haberle, R.M., 2004. Origin and role of water ice clouds in the Martian water cycle as inferred
866 from a general circulation model. *J. Geophys. Res.* 109, E10004.
- 867 Montmessin, F., Gondet, B., Bibring, J.P., Langevin, Y., Drossart, P., Forget, F., Fouchet, T., 2007. Hyper-spectral imaging of convective CO₂ ice
868 clouds in the equatorial mesosphere of Mars. *J. Geophys. Res.* 112. doi:10.1029/2007JE002944.
- 869 Nachbar, M., Duft, D., Mangan, T.P., Martin, J.C.G., Plane, J.M.C., Leisner, T., 2016. Laboratory measurements of heterogeneous CO₂ ice nucleation
870 on nanoparticles under conditions relevant to the Martian mesosphere. *J. Geophys. Res. Planets* 121, 753–769. doi:10.1002/2015JE004978.
- 871 Navarro, T., Madeleine, J.B., Forget, F., Spiga, A., Millour, E., Montmessin, F., Määttänen, A., 2014. Global climate modeling of the martian water
872 cycle with improved microphysics and radiatively active water ice clouds. *J. Geophys. Res.* 119, 1479–1495. doi:10.1002/2013JE004550.
- 873 Neumann, G.A., Smith, D.E., Zuber, M.T., 2003. Two mars years of clouds detected by the mars orbiter laser altimeter. *Journal of Geophysical
874 Research: Planets* 108. doi:10.1029/2002JE001849.
- 875 Pettengill, G.H., Ford, P.G., 2000. Winter clouds over the north Martian polar cap. *Geophys. Res. Lett.* 27, 609–612. doi:[https://doi.org/10.
876 1029/1999GL010896](https://doi.org/10.1029/1999GL010896).
- 877 Plane, J.M.C., Carrillo-Sanchez, J.D., Mangan, T.P., Crismani, M.M.J., Schneider, N.M., Määttänen, A., 2018. Meteoric metal chemistry in the mar-
878 tian atmosphere. *J. Geophys. Res. Planets* , 695–707 URL: <http://dx.doi.org/10.1002/2017JE005510>, doi:10.1002/2017JE005510.
- 879 Pottier, A., Forget, F., Montmessin, F., Navarro, T., Spiga, A., Millour, E., Szantai, A., Madeleine, J.B., 2017. Unraveling the martian water cycle
880 with high-resolution global climate simulations. *Icarus* 291, 82–106. doi:10.1016/j.icarus.2017.02.016.
- 881 Scholten, F., Hoffmann, H., Määttänen, A., Montmessin, F., Gondet, B., Hauber, E., 2010. Concatenation of HRSC colour and OMEGA data for the
882 determination and 3D-parameterization of high-altitude CO₂ clouds in the Martian atmosphere. *Planet. Space Sci.* 58, 1207–1214. URL: [http://
883 www.sciencedirect.com/science/article/pii/S0032063310001170](http://www.sciencedirect.com/science/article/pii/S0032063310001170), doi:<https://doi.org/10.1016/j.pss.2010.04.015>.
- 884 Sefton-Nash, E., Teanby, N., Montabone, L., Irwin, P., Hurley, J., Calcutt, S., 2013. Climatology and first-order composition estimates of mesospheric
885 clouds from mars climate sounder limb spectra. *Icarus* 222, 342 – 356. URL: [http://www.sciencedirect.com/science/article/pii/
886 S0019103512004587](http://www.sciencedirect.com/science/article/pii/S0019103512004587), doi:<https://doi.org/10.1016/j.icarus.2012.11.012>.
- 887 Smith, M.D., 2002. The annual cycle of water vapor on Mars as observed by the Thermal Emission Spectrometer. *Journal of Geophysical Research*
888 107, 5115.
- 889 Spiga, A., González-Galindo, F., López-Valverde, M.Á., Forget, F., 2012. Gravity waves, cold pockets and CO₂ clouds in the Martian mesosphere.
890 *Geophys. Res. Lett.* 39, L02201. doi:10.1029/2011GL050343.
- 891 Stevens, M.H., Siskind, D.E., Evans, J.S., Jain, S.K., Schneider, N.M., Deighan, J., Stewart, A.I.F., Crismani, M., Stiepen, A., Chaffin, M.S.,
892 McClintock, W.E., Holsclaw, G.M., Lefèvre, F., Lo, D.Y., Clarke, J.T., Montmessin, F., Jakosky, B.M., 2017. Martian mesospheric cloud
893 observations by iuvs on maven: Thermal tides coupled to the upper atmosphere. *Geophys. Res. Lett.* 44, 4709–4715. URL: [http://dx.doi.
894 org/10.1002/2017GL072717](http://dx.doi.org/10.1002/2017GL072717), doi:10.1002/2017GL072717. 2017GL072717.
- 895 Titus, T.N., 2005. Mars Polar Cap Edges Tracked over 3 Full Mars Years, in: Mackwell, S., Stansbery, E. (Eds.), 36th Annual Lunar and Planetary
896 Science Conference, p. 1993.
- 897 Tobie, G., Forget, F., Lott, F., 2003. Numerical simulation of the winter polar wave clouds observed by Mars Global Surveyor Mars Orbiter
898 Laser Altimeter. *Icarus* 164, 33–49. URL: <http://www.sciencedirect.com/science/article/pii/S0019103503001313>, doi:[https://doi.org/10.1016/S0019-1035\(03\)00131-3](https://doi.org/10.1016/S0019-1035(03)00131-3).
- 899 Toigo, A.D., Waugh, D.W., Guzewich, S.D., 2017. What causes Mars’ annular polar vortices? *Geophys. Res. Lett.* 44, 71–78. doi:10.1002/
900 2016GL071857.
- 901 Vals, M., Rossi, L., Montmessin, F., Lefèvre, F., Gonzalez Galindo, F., Fedorova, A.A., Luginin, M., Francois, F., Millour, E., Korablev, O.I.,
902 et al., 2022. Improved modeling of mars’ hdo cycle using a mars’ global climate model. *Earth and Space Science Open Archive* , 27 URL:
903 <https://doi.org/10.1002/essoar.10510380.1>, doi:10.1002/essoar.10510380.1.
- 904 Vincendon, M., Pilorget, C., Gondet, B., Murchie, S., Bibring, J.P., 2011. New near-IR observations of mesospheric CO₂ and H₂O clouds on Mars.
905 *J. Geophys. Res.* 116, E00J02. doi:10.1029/2011JE003827.
- 906 Wood, S.E., 1999. Nucleation and Growth of CO₂ Ice Crystals in the Martian Atmosphere. Ph.D. thesis. University of California. Los Angeles.
- 907 Yamashita, T., Odaka, M., ichiro Sugiyama, K., Nakajima, K., Ishiwatari, M., Nishizawa, S., Takahashi, Y.O., Hayashi, Y.Y., 2016. A Numerical
908 Study of Convection in a Condensing CO₂ Atmosphere under Early Mars-Like Conditions. *J. Atmos. Sci.* 73, 4151–4169. URL: <https://doi.org/10.1175/JAS-D-15-0132.1>,
909 doi:10.1175/JAS-D-15-0132.1, arXiv:<https://doi.org/10.1175/JAS-D-15-0132.1>.
- 910 Yiğit, E., Medvedev, A.S., Hartogh, P., 2015. Gravity waves and high-altitude CO₂ ice cloud formation in the Martian atmosphere. *Geophys. Res.*
911 *Lett.* 42, 4294–4300. doi:10.1002/2015GL064275, arXiv:1505.04472.